

T-3315

FRACTURES AND SHEAR VERTICAL SEISMIC PROFILING

by

Richard G. Weber

ARTHUR LAKES LIBRARY
COLORADO SCHOOL of MINES
GOLDEN, COLORADO 80401

ProQuest Number: 10782872

All rights reserved

INFORMATION TO ALL USERS

The quality of this reproduction is dependent upon the quality of the copy submitted.

In the unlikely event that the author did not send a complete manuscript and there are missing pages, these will be noted. Also, if material had to be removed, a note will indicate the deletion.



ProQuest 10782872

Published by ProQuest LLC (2018). Copyright of the Dissertation is held by the Author.

All rights reserved.

This work is protected against unauthorized copying under Title 17, United States Code
Microform Edition © ProQuest LLC.

ProQuest LLC.
789 East Eisenhower Parkway
P.O. Box 1346
Ann Arbor, MI 48106 – 1346

A thesis submitted to the Faculty and the Board of Trustees of the Colorado School of Mines in partial fulfillment of the requirements for the degree of Master of Science in Geophysics.

Golden, Colorado

Date 12/11/86

Signed: Richard G. Weber

Richard G. Weber

Approved: J. E. White

J. E. White,

Thesis Advisor.

Golden, Colorado

Date 12/12/86

Approved: Phillip R. Romig

Phillip R. Romig,

Department Chairman,

Geophysics

Abstract

A laboratory model was constructed to observe the effect of an idealized fracture on the amplitude of the particle displacement due to a shear wave at grazing incidence on the fracture. Particle displacements due to shear waves incident on stress free and linear slip boundaries were then calculated. The empirical amplitudes more closely approximated the stress free case. It was also found, from the theoretical results, that the empirical model did not meet the grazing incidence condition as for this case true grazing occurs at between one to zero degrees and the model was constructed at eighteen degrees.

Table of Contents

	<u>PAGE</u>
ABSTRACT	iii
TABLE OF CONTENTS	iv
LIST OF FIGURES	vi
ACKNOWLEDGEMENTS	xii
I. Introduction	1
II. Description of Specific Problem.	5
III. Physical Model	8
III.1 Theory	8
III.2 Model Materials and Construction .	11
III.3 Setup and Testing.	13
III.3 Experimental Procedure	15
III.4 Preliminary Analysis	22
IV. Stress Free Case	32
IV.1 Mathematical Development of Stress	
Free Boundary.	32
- Displacement Due to Shear	
Waves	32
- Displacement Due to Compress-	
ional Waves	39
IV.2 Application of Stress Free Formu-	
lation	42

	<u>PAGE</u>
IV.3 Numerical Stress Free Results. . .	43
- 72° to 90° Angle of Inci-	
dence	43
- Comparison to Physical	
Experiment.	48
V. Linear Slip Boundary	55
V.1 Mathematical Development	56
V.2 Application of Linear Slip	
Formulation.	61
V.3 Linear Slip Results.	63
VI. Conclusions.	80
REFERENCES	82
Appendix 1 Electronic Components and Final	
Settings.	84
Appendix 2 Fortran 77 Code of Program "SFB". .	85
Appendix 3 Fortran 77 Code of Program "LSLP" .	88

List Of Figures

<u>FIGURE</u>		<u>PAGE</u>
2-1	Problem being investigated .	6
3-1	Schematic of Major Model Components. .	9
3-2	Model with 20° Approximate Wavefront and Partial Grid	17
3-3	Contoured First Break Times. .	18
3-4	Fracture Oriented Coordinate System. .	20
3-5	Generation of Interfering Wavefields .	23
3-6	Recorded Waveform With Reflection Inter- ference	25
3-7	Recorded Waveform Without Reflection Interference	26
3-8	Measured Displacement Amplitude vs. Distance From Fracture, $Y = 2$	27

<u>FIGURE</u>		<u>PAGE</u>
3-9	Measured Displacement Amplitude vs. Distance From Fracture, $Y = 12$. . .	28
3-10	Measured Displacement Amplitude vs. Distance From Fracture, $Y = 20$. . .	29
3-11	Measured Displacement Amplitude vs. Distance From Fracture, $Y = 28$. . .	30
4-1	Graphic Description of Stress Free Boundary Problem	33
4-2	Calculated Normalized Displacement Amplitude, Stress Free Boundary Case, Incident Angle of 72°	44
4-3	Calculated Normalized Displacement Amplitude, Stress Free Boundary Case, Incident Angle of 85°	45
4-4	Calculated Normalized Displacement Amplitude, Stress Free Boundary Case, Incident Angle of 89°	46

<u>FIGURE</u>		<u>PAGE</u>
4-5	Calculated Normalized Displacement Amplitude, Stress Free Boundary Case, Incident Angle of 90°	47
4-6	Comparison of Numerical Stress Free Data and Experimental Data at Y = 2	49
4-7	Comparison of Numerical Stress Free Data and Experimental Data at Y = 12.	50
4-8	Comparison of Numerical Stress Free Data and Experimental Data at Y = 20.	51
4-9	Comparison of Numerical Stress Free Data and Experimental Data at Y = 28.	52
5-1	Graphic Description of Linear Slip Boundary Problem	57
5-2	Calculated Normalized Displacement Amplitude, Linear Slip Interface, $Q = -9.60 \times 10^{-15}$, Incident Angle of 72°	64

<u>FIGURE</u>		<u>PAGE</u>
5-3	Calculated Normalized Displacement Amplitude, Linear Slip Interface, $Q = -9.60 \times 10^{-10}$, Incident Angle of 72°	65
5-4	Calculated Normalized Displacement Amplitude, Linear Slip Interface, $Q = -9.60 \times 10^{-8}$, Incident Angle of 72°	66
5-5	Calculated Normalized Displacement Amplitude, Linear Slip Interface, $Q = -9.60 \times 10^{-7}$, Incident Angle of 72°	67
5-6	Calculated Normalized Displacement Amplitude, Linear Slip Interface, $Q = -9.60 \times 10^{-6}$, Incident Angle of 72°	68
5-7	Calculated Normalized Displacement Amplitude, Linear Slip Interface, $Q = -9.60 \times 10^{-4}$, Incident Angle of 72°	69
5-8	Calculated Normalized Displacement Amplitude, Linear Slip Interface, $Q = -9.60 \times 10^{-15}$, Incident Angle of 85°	72

<u>FIGURE</u>		<u>PAGE</u>
5-9	Calculated Normalized Displacement Amplitude, Linear Slip Interface, $Q = -9.60 \times 10^{-10}$, Incident Angle of 85°	73
5-10	Calculated Normalized Displacement Amplitude, Linear Slip Interface, $Q = -9.60 \times 10^{-8}$, Incident Angle of 85°	74
5-11	Calculated Normalized Displacement Amplitude, Linear Slip Interface, $Q = -9.60 \times 10^{-7}$, Incident Angle of 85°	75
5-12	Calculated Normalized Displacement Amplitude, Linear Slip Interface, $Q = -9.60 \times 10^{-6}$, Incident Angle of 85°	76
5-13	Calculated Normalized Displacement Amplitude, Linear Slip Interface, $Q = -9.60 \times 10^{-4}$, Incident Angle of 85°	77
5-14	Calculated Normalized Displacement Amplitude, Linear Slip Interface, $Q = -9.60 \times 10^{-15}$, Incident Angle of 72° , $W = 265$ Hz .	78

<u>FIGURE</u>		<u>PAGE</u>
5-15	Calculated Normalized Displacement Amplitude, Linear Slip Interface, $Q = -9.60 \times 10^{-15}$, Incident Angle of 72° , $\omega = 5000$ Hz.	79

Acknowledgements

I would like to take this opportunity to thank Drs. J. White, F. Hagin and W. Whitman for assuming the responsibility of serving on my committee. In particular, I must express my appreciation to Dr. White, who spent much time guiding and assisting me through the maze of problems that were encountered during the execution of this project.

I would also like to thank the Borehole Geophysics Project for the financial support that made this project possible.

I. Introduction

Fracture detection and or characterization is a problem which has application in a wide variety of fields. Some common areas of interest are geothermal resources, underground waste disposal, hydrocarbon recovery and non-destructive testing of materials. Numerous authors have described a variety of theoretical and empirical work treating the subject as it relates to their particular field. Within this body of work a few themes are dominant. These deal primarily with the measurement of the amplitude of some wavefield after contact with a fracture zone. We will be consistent with this trend. Our study focuses on the interaction of shear wave energy with a fracture plane in terms of reflection amplitude versus position relative to the fracture.

In 1973 the Geophysical Society of Houston sponsored a symposium on bright spots. Several papers were presented which illustrated ways of relating seismic amplitude changes to lithology and or structure. Hilterman (1975) developed a method which allowed for the estimation of: a) lateral variations in reflection amplitude due to boundary curvature, b) diffraction and reflection interference at pinchouts, and c) amplitude effects due to diffractions from fault edges.

Trorey (1970) studied the effect of various reflector geometries on the generation of diffractions. He found that the response from a laterally discontinuous edge (fault) is laterally continuous. The diffractions behave in such a way as to add to the continuity of the total response. Van der Hijden and Neerhoff (1984) investigated the diffraction of elastic waves by a sub-surface crack. Their work related incident waveform angle to a normalized mode power conversion factor. Aki, et. al (1982) interpreted seismic data from fracturing experiments in terms of scattered wavefields.

In dealing with the more specific problem of detecting fractures within the earth many authors have turned to the zone surrounding or within the borehole. Leary and Henyey (1985) described a method of locating a fracture zone using P-wave velocity profiles. A borehole sensor and an array of shotpoints distributed azimuthally and radially were used. Fehler, et. al (1982) used a compressional and shear wave VSP study to detect the presence of a hydrofrac zone. They concluded that only the shear wave energy was affected by the fractures.

Paillet and White (1982) studied the relationship between acoustic waves and rock properties in the borehole. They constructed amplitude logs which were sensitive to variations in the presence of fluid filled fractures in the

borehole wall and concluded that the simplest measure of fracture properties is given by studying tube wave amplitude. Cheng, Toksöz and Willis (1982) looked at fracture detection in terms of wave attenuation from the study of full waveform acoustic logs. Beydoun, Cheng and Toksöz (1985) theoretically treated the problem of tube wave generation by a non-normally incident compressional wave for an inclined borehole intersecting a tilted parallel wall fracture. They found that tube wave amplitude was dependent upon the permeability and length of the fracture as well as waveform frequency. Crampin (1985) evaluated the orientation of fractures by using a polarized shear source and three component downhole detectors.

In this study we examine the effect of a fracture on the amplitude of a reflected SV wavefield. SV waves were chosen because for the specific problem geometry used, these waves are attenuated by the presence of a fracture. By contrast, SH waves would give near perfect reflection at grazing incidence. The difference is due to the orientation of the particle displacements of the two wavefields with respect to the fracture plane.

First, we empirically demonstrate the presence of a fracture in an elastic solid using shear wave energy. A theoretical treatment of shear wave reflection from a stress free boundary follows, in an attempt to numerically reproduce

the empirical results. We then turn to a model which more accurately describes a fracture within the earth. The basis for this begins with Schoenberg's (1980) description of a linear slip interface. The theory is expanded to allow for study of energy incident upon a fracture beyond the critical angle. We then compare these results with that of the stress free case.

II. Description of Specific Problem

The objective of this study is to physically and numerically model the situation whereby a shear wavefield encounters a fracture during propagation. Figure 2-1 graphically describes the specific problem modeled. A borehole exists in the vicinity of a high angle (nearly vertical) fracture. Shear waves (SV) are generated at the surface and are eventually reflected off the interface created by the fracture. Measurements of the particle displacement due to the reflections are made by detectors in the borehole. If we can imagine a series of boreholes, evenly spaced, in line, and extending for some distance away from the fracture it would be possible to construct a profile of reflection amplitude vs. distance from the fracture. Obviously this is not a practical configuration to actually implement, however in the lab and numerically it is quite simple.

In order to simplify the problem the case studied will be that of a single layered earth. The fracture will then be a discontinuity within this layer and must be characterized in some manner. This characterization of the fracture is what results in two distinct cases. The first is the stress free case and the second, the linear slip case. Each of

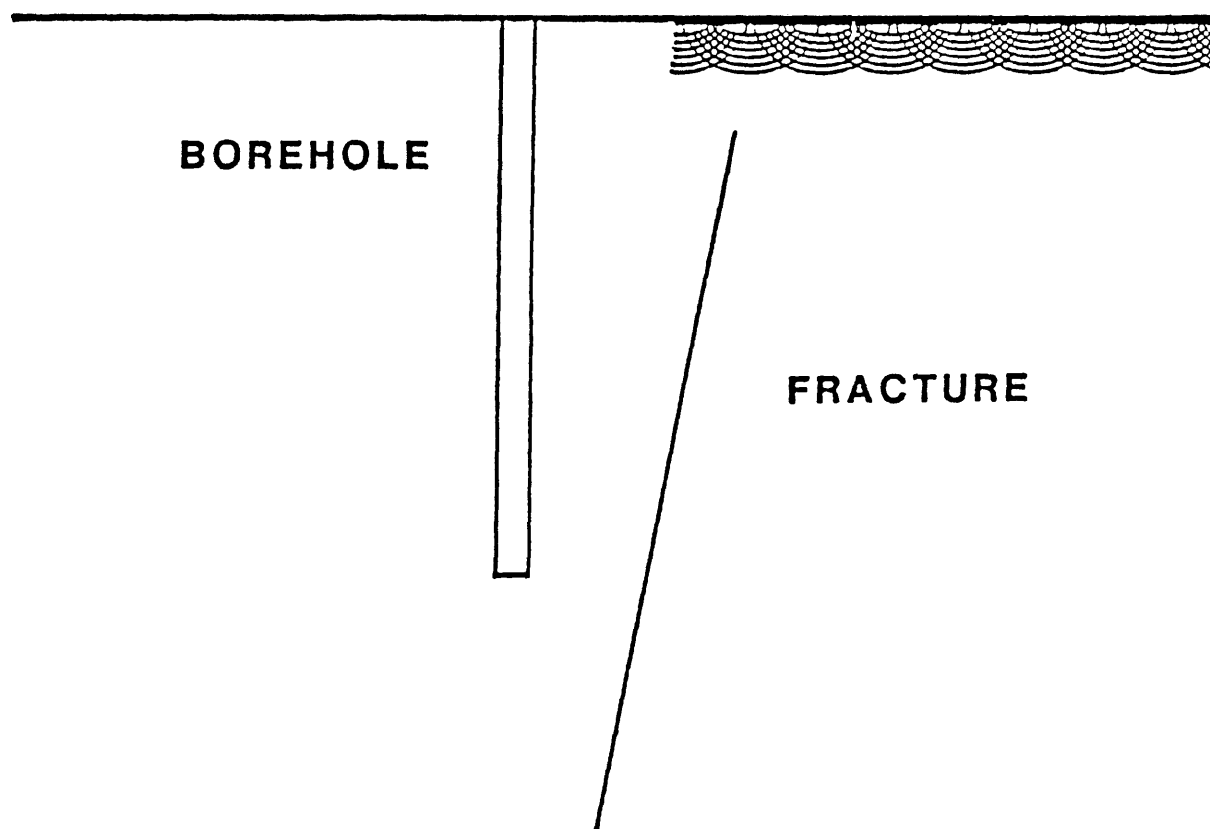


Figure 2-1

Problem being investigated

these is developed numerically and the lab model's design is such that it more closely describes the stress free case.

III. Physical Model

III.1 Theory

Figure 3-1 is a simple schematic of the main components of the lab apparatus. A single layered earth is modeled by a piece of plexiglas. The energy source consists of a compressional wave transducer bonded to the end of an aluminum bar to which the plexiglas is attached. A pulse generator excites the transducer sending compressional waves down the length of the bar. Huygen's principle states that points along the bar will act as new point sources and radiate energy into the plexiglas. This energy will propagate normal to wavefronts which are at an angle $\theta = \sin^{-1}(V_s/V_p)$ with the bar, where V_s = shear velocity in plexiglas and V_p = compressional velocity in aluminum. Since θ is relatively small and the compressional motion is parallel to the length of the bar, the principal particle motion in the plexiglas will be parallel to the wavefronts, resulting in shear waves within the plexiglas.

The wavefronts are now assumed to represent a parallel to the earth's surface. Knowing θ then allows the positioning of a fracture at the desired angle. This angle is chosen such that it results in a high angle fracture with

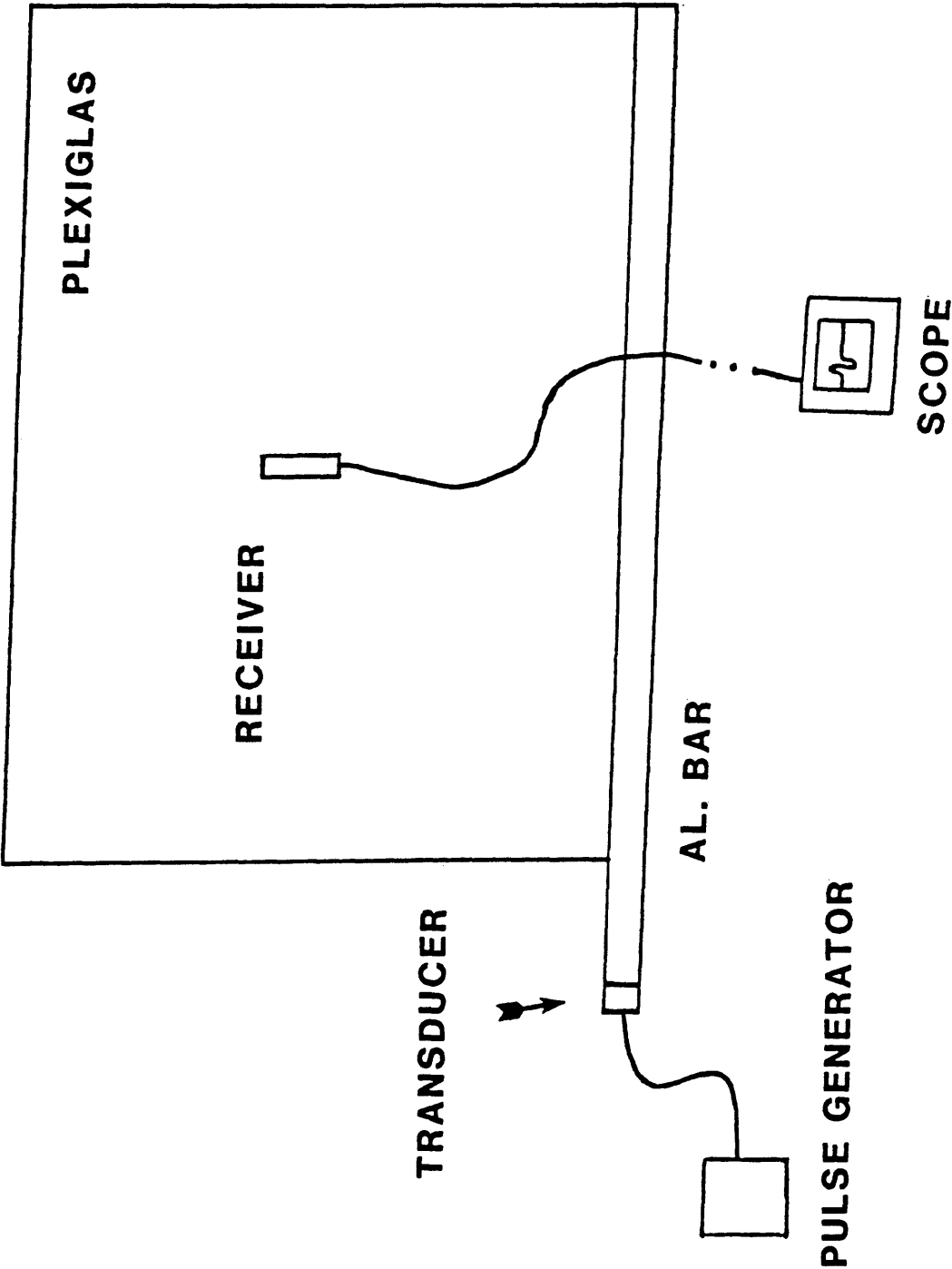


Figure 3-1
Major Model 1 Components

respect to the wavefronts (earth surface) within the plexiglas.

After fracturing, measurements of particle displacement are made, within the plexiglas. Downhole shear detectors are represented by a mono-phonograph cartridge. This cartridge is sensitive to horizontal (shear) motion only, which is precisely what exists in the plexiglas. The cartridge translates particle motion into an output voltage which is then filtered and amplified. A digital oscilloscope displays the final waveform, allowing for measurement of amplitude and arrival time of the first break energy. These measurements are distributed spatially so as to represent downhole measurements at various depths and distances from the fracture. Amplitude profiles of the reflection energy as a function of distance from the fracture can then be constructed.

III.2 Model Materials and Construction

Figure 3-1 illustrates some of the main components of the model. A 4' x 7' sheet of 1/8" plexiglas is the single layered earth in which the wave behavior will be studied. This sheet was joined to a 3/4" x 3/4" x 8' aluminum bar by means of a 1/8" x 1/4" x 7' slot machined into the bar. The slot was filled with epoxy cement and the plexiglas inserted into it. This procedure provided an excellent bond between these components, therefore allowing waveform changes to be attributed solely to the fracture.

Attached to one end of the bar, by epoxy cement, is a crystal compressional wave transducer. The transducer is wired with coaxial cable which connects it to a pulse generator. The generator will output a square wave pulse which can be adjusted for length of duty cycle and amplitude, as well as trigger position.

To receive the transmitted energy, a mono-phonograph cartridge was used. The cartridge translates the detected motion into a small output voltage, which is then routed into a stereo amplifier, wired for one channel. The amplifier provides needed gain to the output voltage. After gain, the signal is passed through an adjustable dual electronic filter configured to function as a bandpass filter.

The final waveform is then displayed on a digital oscilloscope, from which amplitude and arrival time can be measured. Full waveform plots can also be made by an X-Y pen plotter connected to the oscilloscope.

III.3 Set-up and Testing

Construction and set-up of materials which dealt with the transmitted signal was trivial. However, this was not the case with those components dealing with the received signal. Considerable signal to noise ratio problems were encountered which had to be overcome before any data could be recorded.

Assembly of the model components was done in the basement of the Cecil & Ida Green Center at the Colorado School of Mines. The room used was next to a room containing a large amount of computer hardware and its associated cooling system. This situation led to the transmission of a large amount of low-frequency noise through the floor which was picked up by the model receiver. An attempt to attenuate this energy was made by placing 1" thick acoustic dampening foam between the model and the table. Significant S/N improvement was made, however more work was required.

Numerous attempts at building R-C bandpass filters were made with varying degrees of success. Significant S/N improvement was made upon acquisition of an adjustable dual electronic filter from the CSM Physics Department. This device consists of two separate filters which were run in series, one as a high pass, one as a low pass giving the effect of a bandpass filter. Pass frequency adjustment is

accomplished by simply turning a couple of dials, and therefore allowed for quick and precise fine tuning of the received signal. After extensive testing, a few of the noise sources were identified as:

- 1) Very low frequency physical vibration, probably due to adjacent cooling equipment.
- 2) High levels of 60 Hz noise due to large amounts of electrical equipment and lighting in area.
- 3) Significant amounts of very high frequency (above 5000 Hz) noise. This led to the signal having a chattered appearance and therefore being very difficult to get reliable amplitude measurements.

The source of this noise was not identified.

It was finally determined that a bandpass filter with 100% corner frequencies of 300 and 5000 Hz resulted in an optimum signal. (Appendix 1 lists all electronic components and final settings.)

III.4 Experimental Procedure

The procedure for the experiment was as follows:

- 1) Determine angle wavefront makes with bar.
- 2) Use wavefront orientation to determine fracture position.
- 3) Set up appropriate coordinate system.
- 4) Collect data, unfractured case.
- 5) Fracture plexiglas.
- 6) Collect data, fractured case.

The wavefront angle θ is given by $\theta = \sin^{-1}(V_s/V_p)$. Therefore to numerically determine θ one needs velocity measurements in both the aluminum and plexiglas.

Compressional velocity measurement in the aluminum was simple. First break times were recorded at several positions along the bar's length. Dividing the difference in position of two points by the difference in arrival time gives the velocity. Times were recorded at three positions, and the velocities calculated were averaged to give a velocity of 15984 feet per second. This compares favorably with a handbook value of 16000 feet per second.

Velocity measurement in the plexiglas is not as trivial as in the aluminum. Propagation direction, in the bar, was already known, we measured along its length which represents a ray, normal to the compressional wavefronts. Orientation

of wavefronts in the plexiglas is unknown, therefore impossible to measure along a raypath.

An initial attempt to determine θ was made by using a handbook value for the shear velocity. The wavefront angle calculated to be 20° . If this is correct, arrival times along a line 20° from the bar should be equal. To test this, measurements were made along such a line, Figure 3-2. Repeated attempts failed to yield a situation where more than two points could be placed along any straight line. Suspicion developed that the plexiglas was dispersive for the bandwidth of energy being used. Another approach was tried.

A grid was laid out by sliding a large piece of graph paper between the plexiglas and the foam (partially shown in Figure 3-2). Arrival times were recorded over the entire sheet at 4" intervals in both directions. An isochron map was then constructed, Figure 3-3. The contours of the map represent shear wavefronts. It is obvious that some irregularities exist, especially near the model edges. It was decided that attempts to measure shear velocity be stopped and to accept the isochron as an accurate representation of energy propagation within the sheet. Fracture location was determined by selecting an area that had reasonably flat, parallel contours and was far from model edges. Fracture orientation was chosen so that the model would represent a case whereby shear energy was at grazing incidence. A value

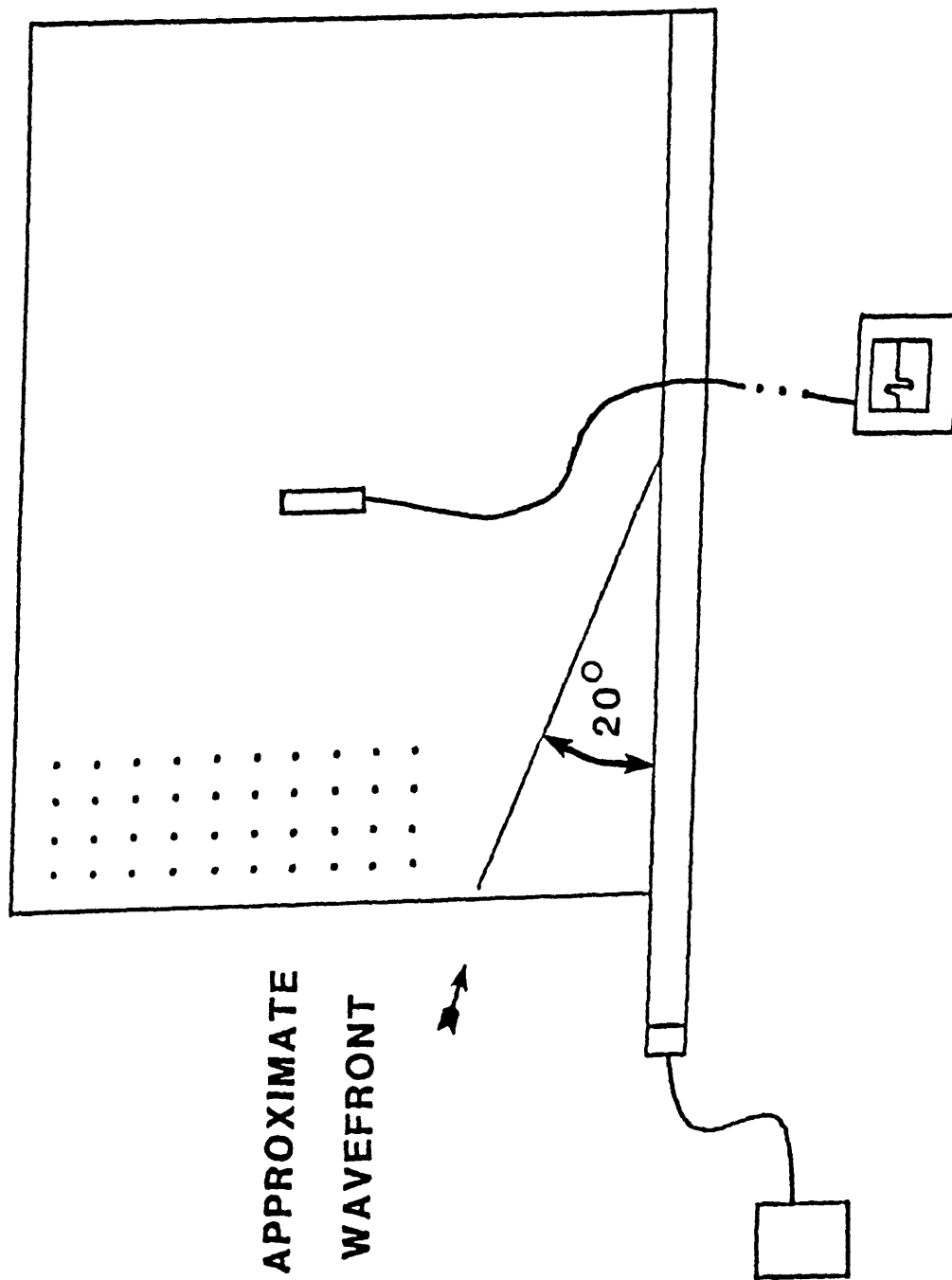


Figure 3-2

Model With 20° Approximate Wavefront and Partial Grid Shown.

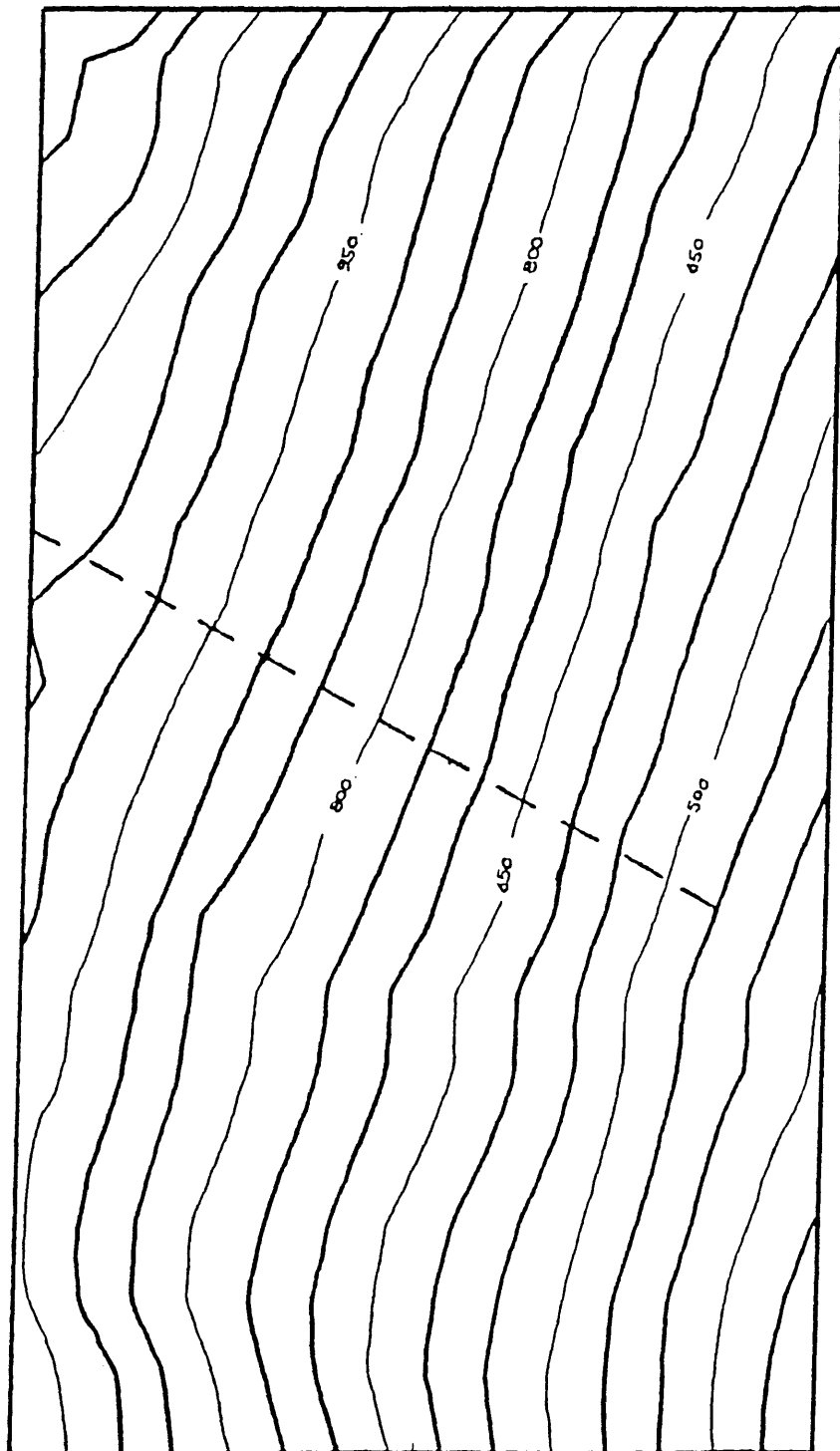


Figure 3-3

Contoured First Break Times. C.I. = 50 Microseconds.

of 72° (90° represents fracture normal to wavefront) was arbitrarily chosen. The dashed line, Figure 3-3, illustrates future fracture position.

With fracture location determined, a coordinate system oriented with respect to the fracture was set up. A piece of graph paper was inserted between the plexiglas and foam such that the grid was square with a line representing the fracture. The grid extended 24" on one side of the fracture and 40" along its length, with the x and y directions labeled as normal and tangential to the fracture, respectively, Figure 3-4.

Data collection for the unfractured case could now begin. Measurements of the waveform in the unfractured plexiglas were necessary to provide control against which the effect of the fracture on the waveform could be measured. Amplitude and arrival time were recorded for the component of motion normal to the fracture line. Rotation of the receiver cartridge allowed for detection of the appropriate component of particle motion. Data were collected over the entire grid at 2" increments with the exception of the region within 4" of the fracture. In this region sampling was done at 1" increments in the x direction.

A fracture was then put in the plexiglas sheet. This was done by cutting a slit along the line on the sheet with a jig saw. Data collection, as described above, was repeated

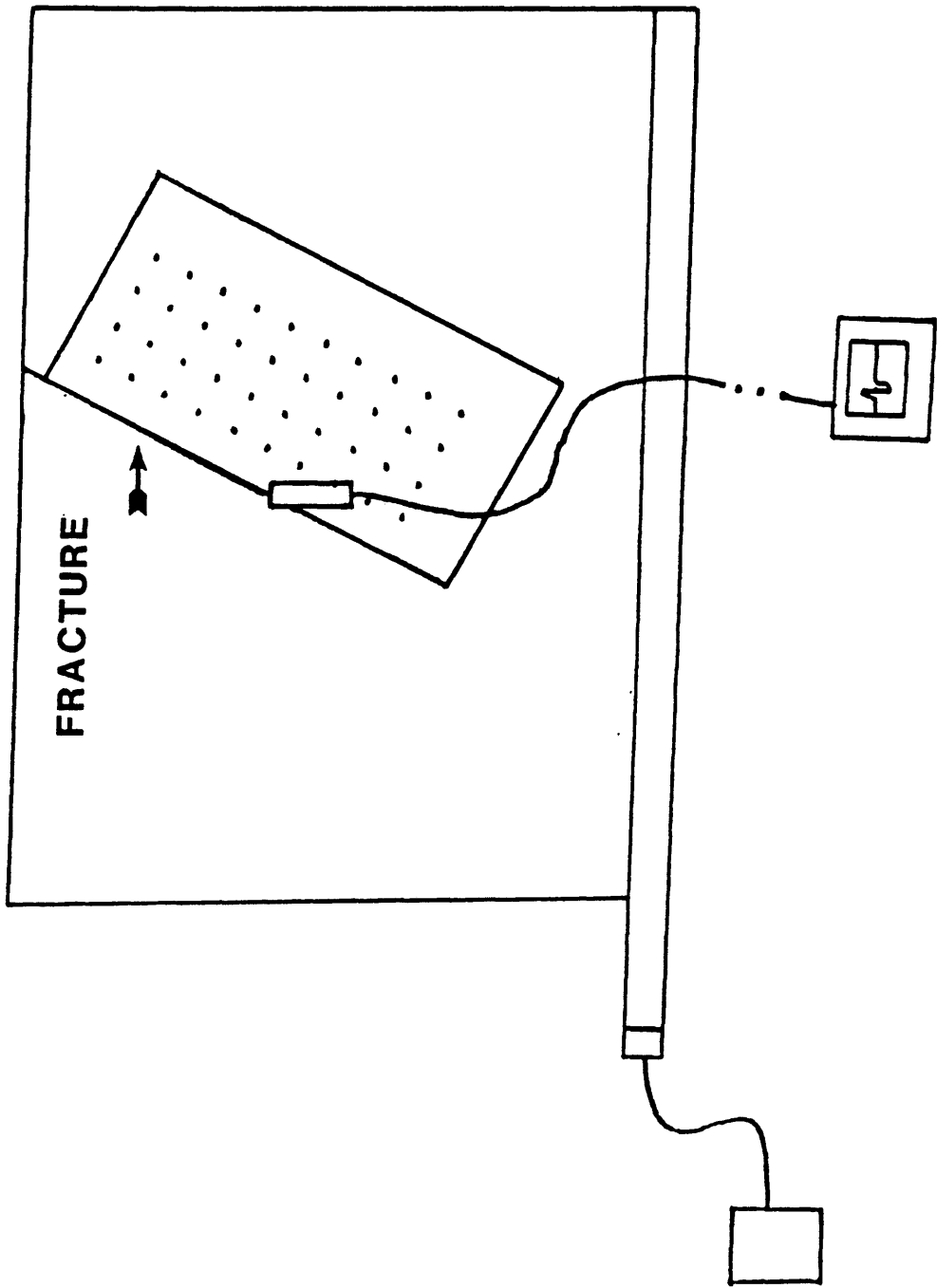


Figure 3-4
Fracture Oriented Coordinate System Used in Locating
Amplitude Measurement Points.

with one exception. Along the profile $Y = 12$ sampling was done at a .2 inch increment in X within two inches of the fracture.

III.4 Preliminary Analysis

In order to be certain that any waveform amplitude changes detected are induced solely by the fracture, certain factors which can also induce amplitude anomalies must be dealt with effectively.

One such factor is the coupling between the plexiglas and the bar. It is obvious that if this joint does not remain constant the transfer of energy from bar to plexiglas will change and a corresponding waveform change may result. We believe that this problem was effectively dealt with by first, ensuring a tight fit between plexiglas and bar through use of a precision machined slot and secondly, not moving the model once the joint was made, therefore eliminating the possibility of breakage.

Another factor that will influence the amplitude of first break energy is reflection interference off model edges or the rebound of compressional energy at the bar end, resulting in another shear wave traveling in the opposite direction as the first, Figure 3-5. These additional wavefields could result in positive or negative adjustments in measured first break energy. It is then clear that an area be determined which will allow for first arrival energy to be measured exclusively.

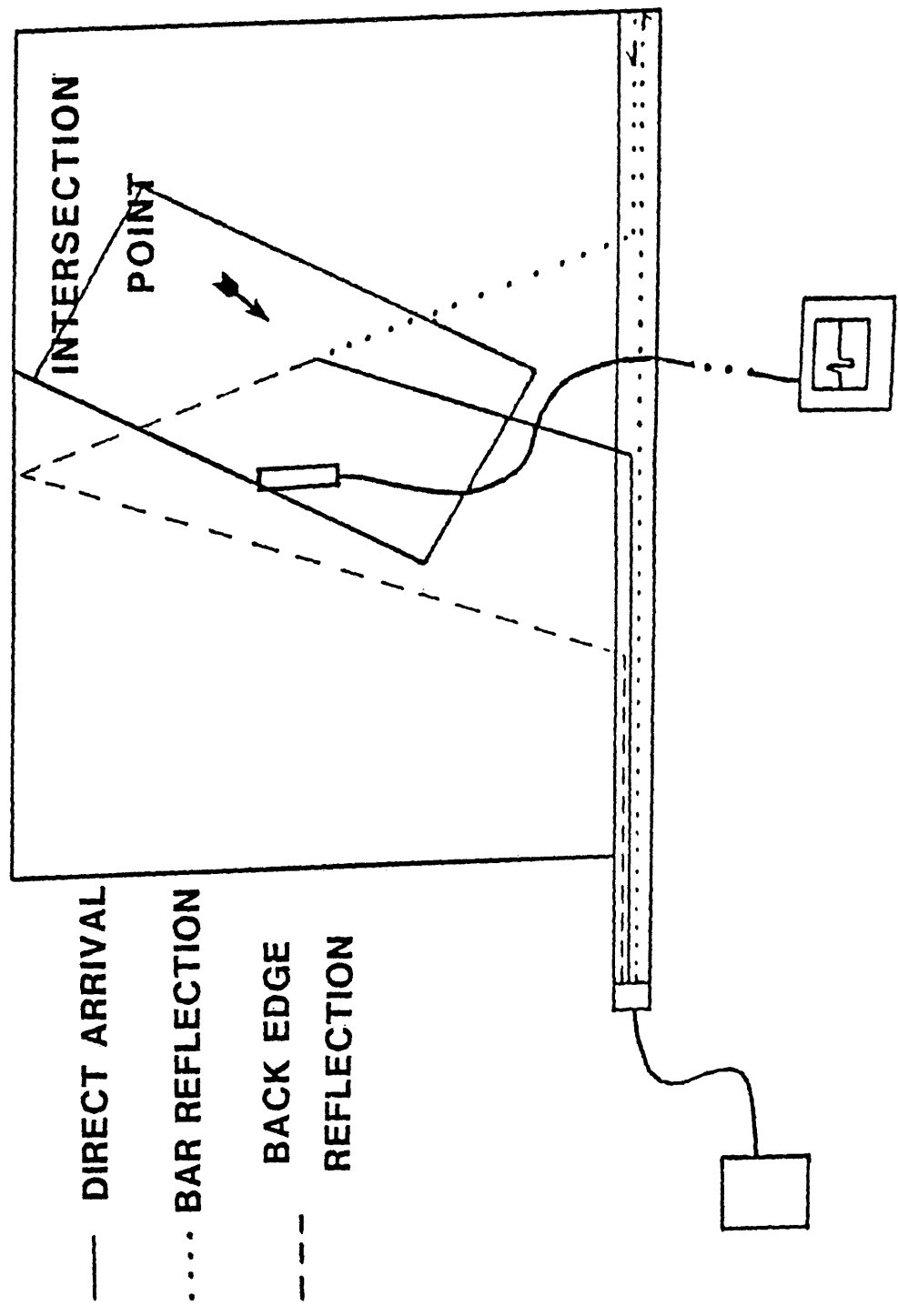


Figure 3-5
Illustration of Wavefields Which Could Interfere With
First Break Amplitudes.

Calculation of such a zone requires that the shear wave velocity be known. To determine shear speed, tangents were drawn to the isochron curves, Figure 3-3, to represent wavefronts. Arrival time was measured along normals to the wavefront lines. From these measurements an average shear speed of 3608 feet/second was calculated.

Ray theory was then applied to calculate arrival times for the reflection off the back plexiglas edge and the bar rebound, for points at which first break amplitude and arrival time had been recorded. If secondary waves arrived at any point before one cycle of the first arrival was complete the data recorded for this point was discarded. (Compare Figures 3-6 and 3-7.) From these calculations it was determined that all data having coordinates $X = 0-12$ and $Y = 0-30$ are unaffected by reflected wavefields.

Four profiles along lines normal to the fracture were then constructed, Figures 3-8 to 3-11. These plots illustrate the change in recorded first break amplitude vs. distance in feet from the fracture. Amplitude values were normalized by dividing post fracture amplitudes by pre-fracture amplitudes which were taken to represent the amplitude of the incoming wave. Distance in all plots is in feet.

From these plots the expected drop in amplitude near the fracture zone is not seen, in fact the opposite effect is

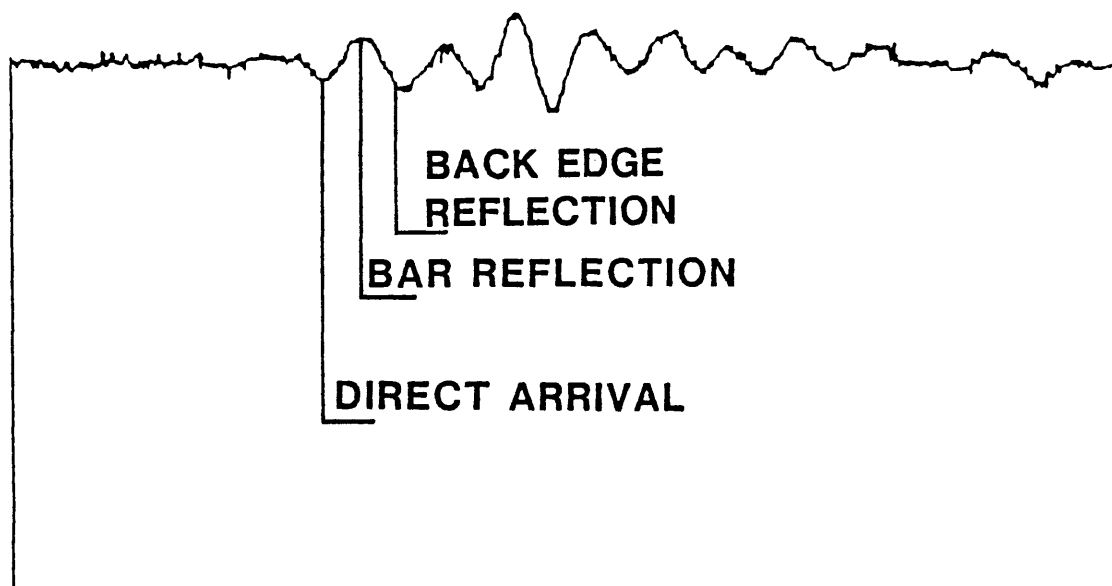


Figure 3-6
Recorded Waveform Illustrating Interference of Reflected
Waveforms with First Break Energy

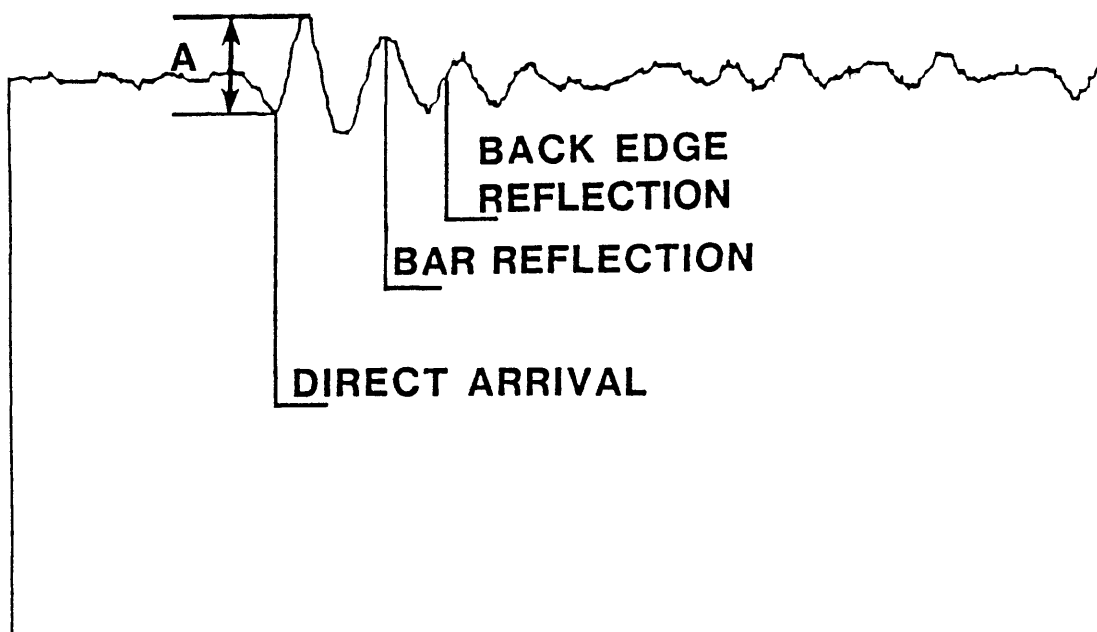


Figure 3-7

Recorded Waveform Illustrating Point Where Reflected Wavefields Do Not Interfere With First Break Energy.

A = Measured First Break Amplitude.

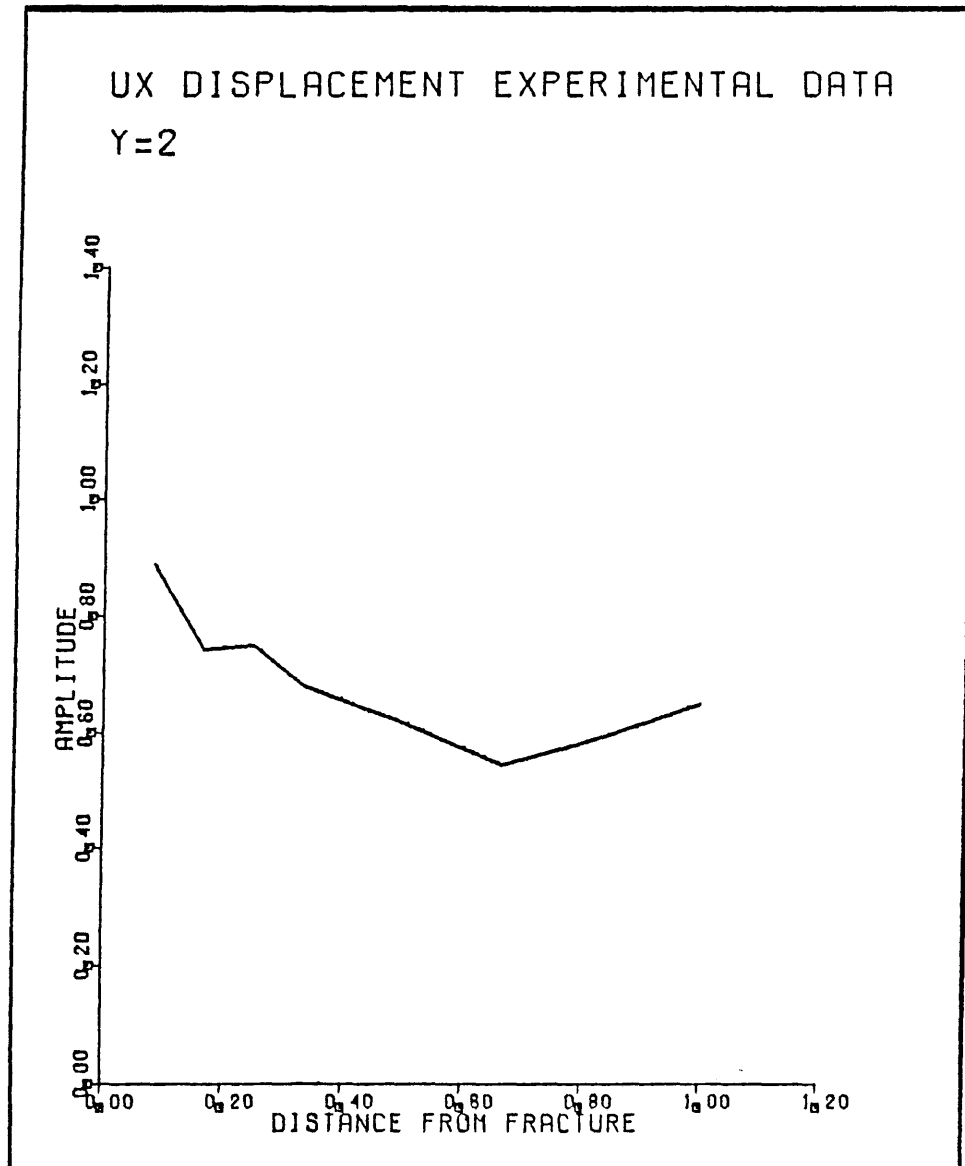


Figure 3-8

Measured Normalized Displacement Amplitude vs.

Distance From Fracture. Profile at Y=2.

ARTHUR LAKES LIBRARY
COLORADO SCHOOL of MINES
GOLDEN, COLORADO 80401

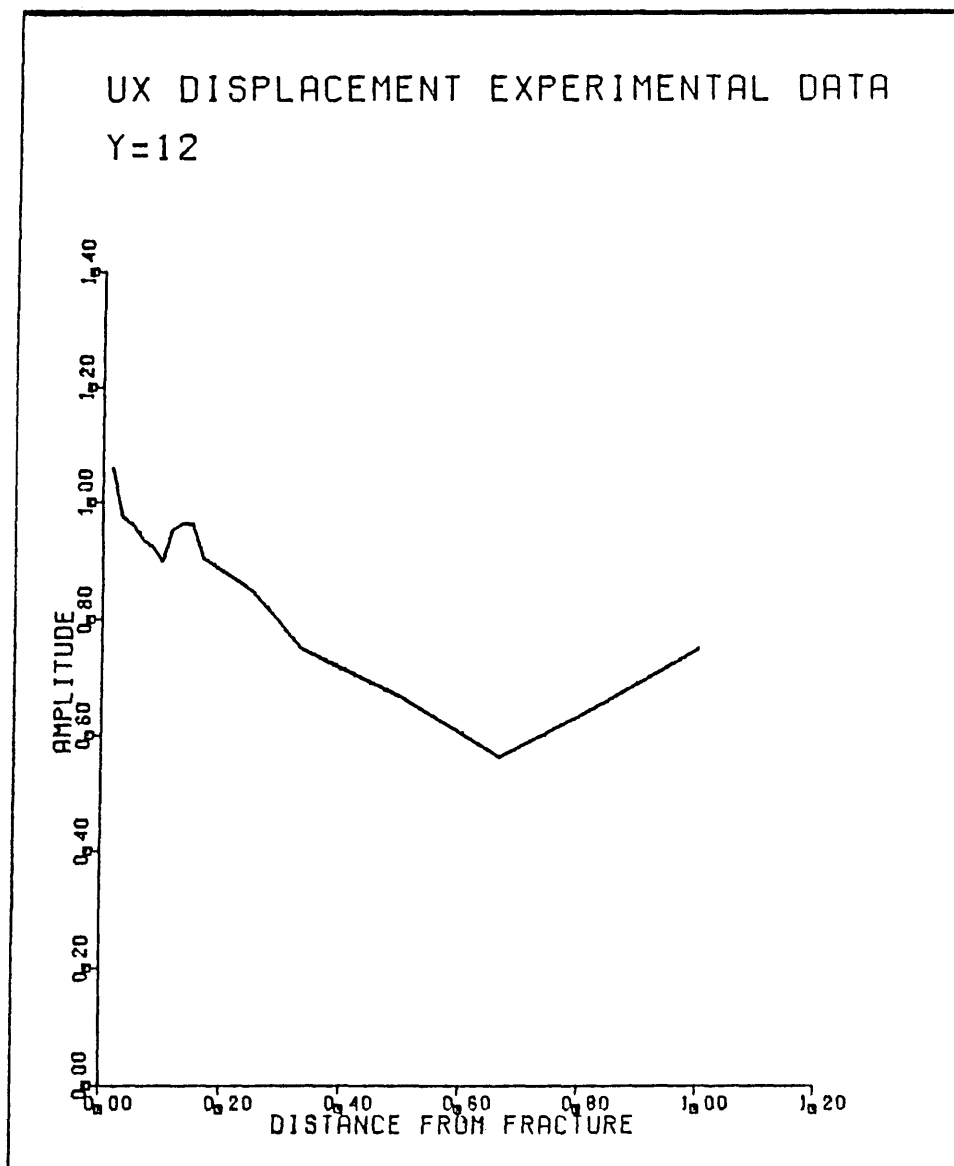


Figure 3-9

Measured Normalized Displacement Amplitude vs.
Distance From Fracture. Profile at Y=12.

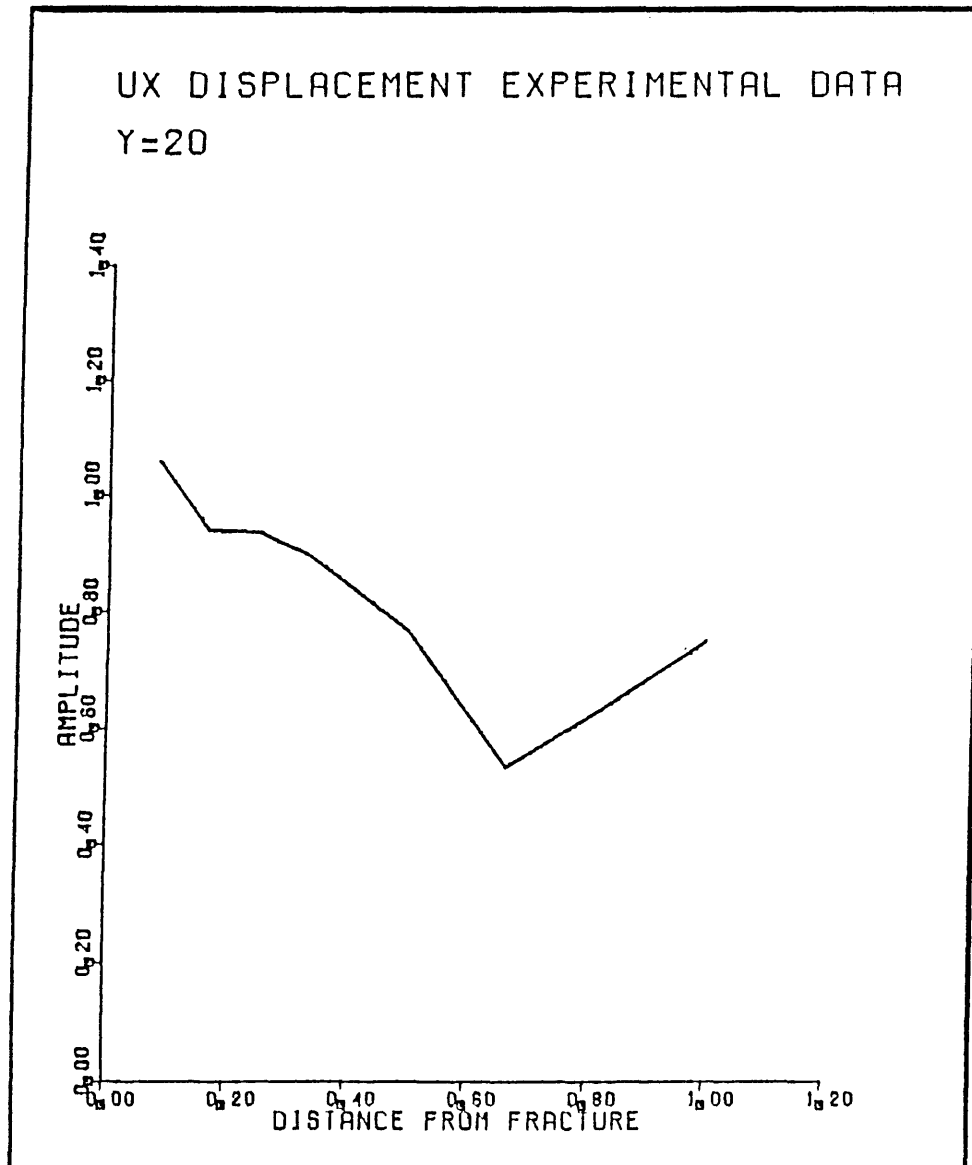


Figure 3-10

Measured Normalized Displacement Amplitude vs.
Distance From Fracture. Profile at Y=20.

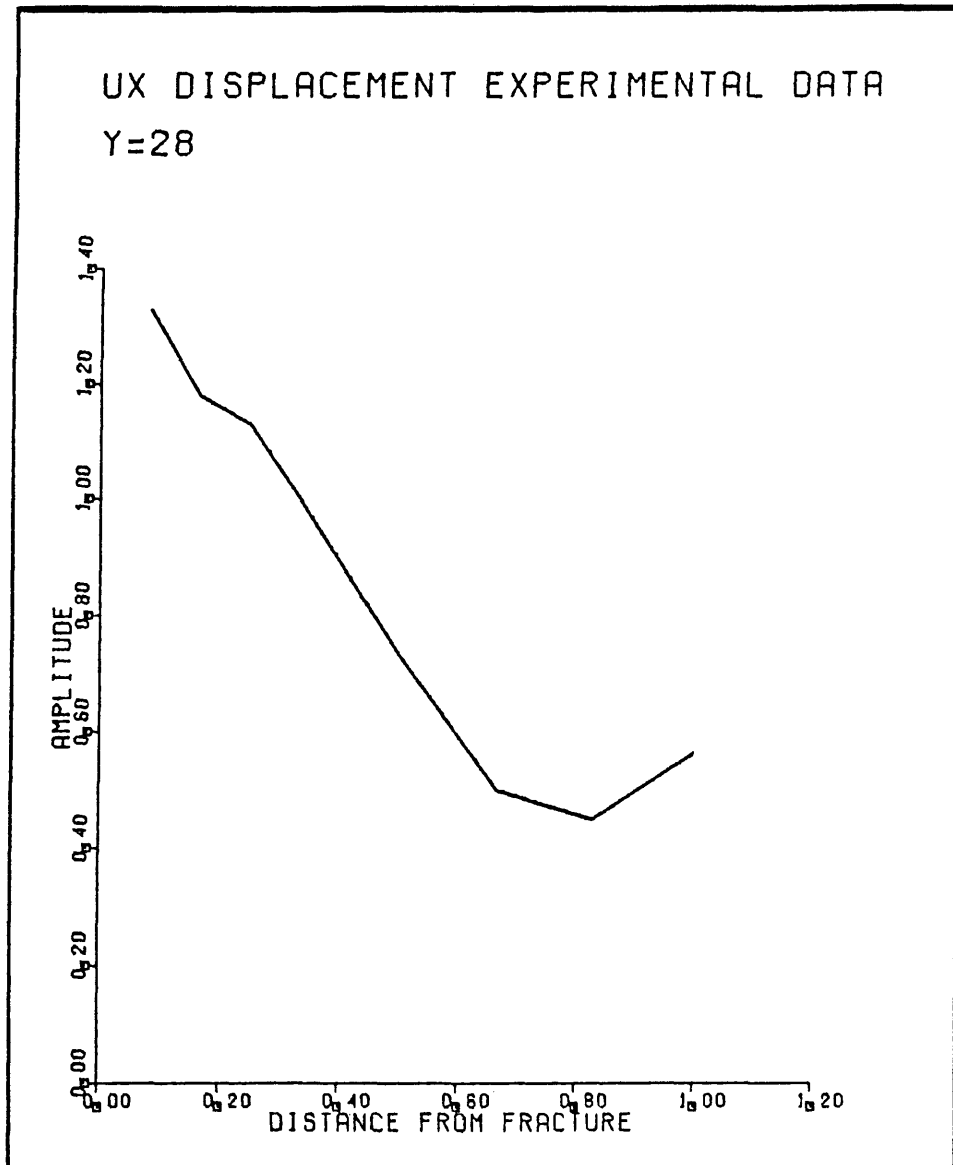


Figure 3-11

Measured Normalized Displacement Amplitude vs.
Distance From Fracture. Profile at Y=28.

observed. On each profile amplitude increases as one nears the fracture. Clearly a more complicated phenomenon is occurring than was expected. Several attempts to explain this anomaly were made without avail and it wasn't until mathematical development of the stress free case was complete that a satisfactory explanation of this phenomenon was developed. It is therefore prudent to delay addressing this problem until a later time.

IV. Stress Free Case

In the physical model the fracture was created by cutting a slot in the plexiglas with a jig saw. The fracture which resulted had no points of contact along its length. Therefore it is practical to model this situation numerically as a stress free boundary.

IV.1 Mathematical Development of Stress Boundary Case.

Displacement Due to Shear Waves

Figure 4-1 illustrates the case we investigate. An incoming shear wave B_1 is incident on a stress free boundary which lies in the yz plane, with incident angle γ_s . A_2 and B_2 represent the reflected compressional and shear wave, respectively. If we constrain B_1 to traveling in the xz plane the compressional and shear waves generated upon reflection at the boundary allow us to consider solutions independent of Y and for which $U_y = 0$. Since we consider cases of near grazing incidence it is appropriate to start with White's (1983) second case treatment of reflection from a stress free boundary, specified by the condition:

$$\beta < |c| < \alpha$$

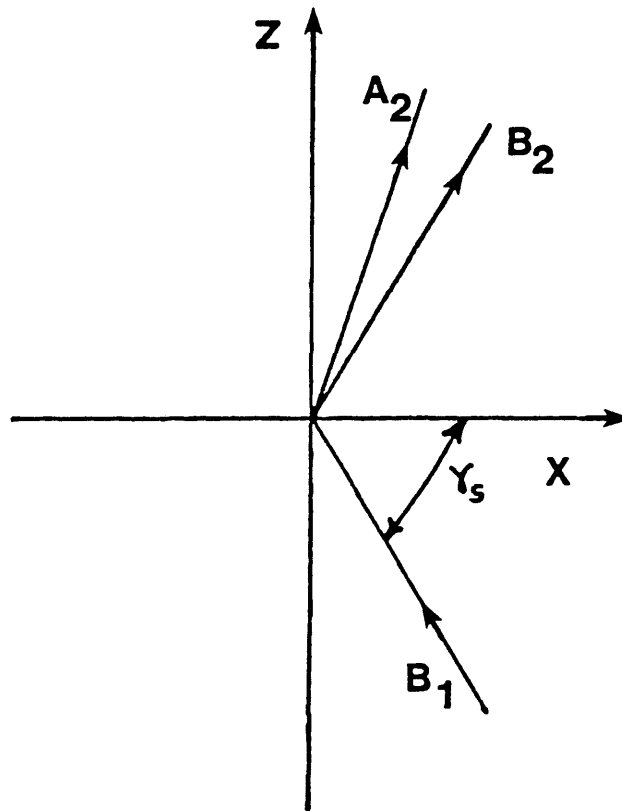


Figure 4-1

Wavefields Studied at Stress Free Boundary.

where β = shear speed, α = compressional speed and c = apparent shear speed along the z axis. In terms of β , the apparent velocities along the z and x axes are:

$$c = \beta / \sin \gamma_s \quad (4-1)$$

$$\beta x = \beta / \cos \gamma_s \quad (4-2)$$

If we consider this velocity range the potential for an incoming shear wave modified from White (1983) equation (2-40) is:

$$\psi_i = (1/2\pi) \int_{-\infty}^{\infty} B_1 e^{ikx} e^{-i\omega z/c} e^{i\omega t} d\omega \quad (4-3)$$

$$\text{where } k = \omega(1/\beta^2 - 1/c^2)^{1/2} \quad (4-4)$$

Substitution in k for c in terms of β gives:

$$k = \omega/\beta x \quad (4-5)$$

and the incident shear potential becomes:

$$\psi_i = (1/2\pi) \int_{-\infty}^{\infty} B_1 e^{i\omega x/\beta x} e^{-i\omega z/c} e^{i\omega t} d\omega \quad (4-6)$$

Now let,

$$B_1 = B\pi[\delta(\omega - \omega_0) + \delta(\omega + \omega_0)] \quad (4-7)$$

Upon substitution and integration, the shear potential is:

$$\psi_i = \frac{1}{2}B[e^{i\omega_0 x/\beta x} e^{-i\omega_0 z/c} e^{i\omega_0 t} + e^{-i\omega_0 x/\beta x} e^{+i\omega_0 z/c} e^{-i\omega_0 t}] \quad (4-8)$$

and simplifying:

$$\psi_i = B\cos(\omega_0 x/\beta x - \omega_0 z/c + \omega_0 t). \quad (4-9)$$

From this expression the displacement in the x and z directions due to the incident shear wave can be computed. From White (1983) equation (2-22):

$$U_{xi} = -\partial\psi_i/\partial z \quad (4-10)$$

$$U_{zi} = \partial\psi_i/\partial x \quad (4-11)$$

at $x = z = 0$:

$$U_{xi} = \omega_0 B/c \sin\omega_0 t \quad (4-12)$$

$$U_{zi} = -\omega_0 B / \beta x \sin \omega_0 t \quad (4-13)$$

and therefore the total displacement due to the incoming shear wave is:

$$U_i = [U_{xi}^2 + U_{zi}^2]^{\frac{1}{2}} = \omega_0 B / \beta \quad (4-14)$$

To compute total shear displacement in the media we must include the reflected shear wave. White (1983) expressed this as:

$$\psi_Y = (1/2\pi) \int_{-\infty}^{\infty} [B_1 e^{ikx} + B_2 e^{-ikx}] e^{-i\omega z/c} e^{i\omega t} d\omega \quad (4-15)$$

Again substitution for k , B_1 , and noting that from White (1983) eq (2-40),

$$B_2 = B_1 e^{i\theta_6} \operatorname{sgn} \omega \quad (4-16)$$

(See (4-24) for θ_6 definition)

we have upon integration:

$$\begin{aligned} \psi_Y = \frac{1}{2} B \{ & [e^{i\omega_0 x / \beta x} e^{-i\theta_6/2} + e^{-i\omega_0 x / \beta x} e^{i\theta_6/2}] \\ & e^{i\omega_0(t-z/c)} e^{i\theta_6/2} + [e^{-i\omega_0 x / \beta x} e^{i\theta_6/2} \\ & + e^{i\omega_0 x / \beta x} e^{-i\theta_6/2}] e^{-i\omega_0(t-z/c)} e^{-i\theta_6/2} \} \quad (4-17) \end{aligned}$$

$$\psi_Y = 2B \cos(\omega_0 x / \beta x - \theta_6 / 2) \cos[\omega_0(t - z/c) + \theta_6 / 2] \quad (4-18)$$

Now since we are only interested in the displacement normal to the boundary, computation of U_x is all that is required. Using equation (2-22) from White (1983),

$$U_{xs} = -\partial \psi_Y / \partial z \quad (4-19)$$

and at $z = 0$

$$U_{xs} = -2B \omega_0 / c \cos(\omega_0 x / \beta x - \theta_6 / 2) \sin(\omega_0 t + \theta_6 / 2)$$

If we normalize this expression with the incident displacement at, $z = 0$:

$$U_{xs} / U_i = -2 \sin \gamma_s \cos(\omega_0 x / \beta x - \theta_6 / 2) \sin(\omega_0 t + \theta_6 / 2) \quad (4-20)$$

To simplify, from White (1983) equation (2-41),

$$e^{i\theta_6} = -(a + ib) / (a - ib) \quad (4-21)$$

$$\text{where } a = (1/\sin^2\gamma_s - 2)^2 \quad (4-22)$$

$$\text{and } b = 4(1 - \beta^2/\alpha^2 \sin^2\gamma_s)^{\frac{1}{2}}(1/\sin^2\gamma_s - 1)^{\frac{1}{2}} \quad (4-23)$$

therefore:

$$\theta_6/2 = \tan^{-1} b/a + \pi/2 \quad (4-24)$$

$$\text{Letting } Q = \tan^{-1} b/a \quad (4-25)$$

and using $-\pi/2$, the final expression for normalized displacement due to shear waves at $z=0$ is:

$$U_{xs}/U_i = -2\sin\gamma_s \sin(\omega_0 x/\beta x - Q) \cos(\omega_0 t + Q) \quad (4-26)$$

In the limit of $\gamma_s \rightarrow \pi/2$ (4-23) is rearranged as:

$$b = 4(\sin^2\gamma_s - \beta^2/\alpha^2)^{\frac{1}{2}} (1 - \sin^2\gamma_s)^{\frac{1}{2}} \quad (4-27)$$

and we see that b is proportional to γ_s itself. Therefore Q is also dependent on γ_s alone. At $x = 0$ (4-26) then becomes:

$$U_{xs}/U_i = -2\sin\gamma_s \sin(-Q) \cos(\omega_0 t + Q) \quad (4-28)$$

and from this we conclude that in the limit of grazing incidence, the amplitude at the boundary is dependent only on the incident angle.

Displacement Due to Compressional Waves

Upon reflection of the incident shear wave at the boundary some mode conversion will occur resulting in the generation of a reflected compressional wave. By symmetry this wave will also have its displacement in the xz plane. Therefore in order to develop a complete expression for the displacement we must consider the contribution from the compressional energy.

As with the reflected shear potential (4-16), White (1983) showed the reflected compressional potential could be expressed in terms of the incident shear energy as:

$$A_2 = B_1 K_5 e^{i\theta_5 \text{sgnw}} \quad (4-29)$$

(See 4-36) for θ_5 definition)

Upon elimination of the incident compressional potential in equation (2-40) White (1983), along with substitution of (4-27) and (4-7) into this expression, integration yields the compressional potential as:

$$\phi = K_5 B e^{-\bar{m}x} \cos[\omega_0(t-z/c) + \theta_5] \quad (4-30)$$

Application of (2-22) White (1983) then yields the displacement:

$$U_{xp} = \partial\phi/\partial x \quad (4-31)$$

at $z=0$

$$U_{xp} = -\bar{m}K_5 B e^{-\bar{m}x} \cos(\omega_0 t + \theta_5) \quad (4-32)$$

Normalizing to the incident shear wave then gives:

$$U_{xp}/U_i = -K_5 \bar{m}\beta/\omega_0 e^{-\bar{m}x} \cos(\omega_0 t + \theta_5) \quad (4-33)$$

To simplify, from White (1983):

$$K_5 = d/(a^2 + b^2)^{1/2} \quad (4-34)$$

where

$$d = 4(1/\sin^2\gamma_s - 1)^{1/2}(1/\sin^2\gamma_s - 2) \quad (4-35)$$

and

$$\theta_s = \tan^{-1}(b/a) + \pi \quad (4-36)$$

or as in (4-25)

$$\theta_s = Q + \pi \quad (4-37)$$

Therefore the final expression for normalized compressional displacement at $z = 0$ is:

$$\begin{aligned} U_{xp}/U_i &= K_5 (\sin^2 \gamma_s - \beta^2/\alpha^2)^{1/2} \\ &\quad e^{-w_0 (\sin^2 \gamma_s - \beta^2/\alpha^2)^{1/2} x/\beta} \\ &\quad \cdot \cos(w_0 t + Q) \end{aligned} \quad (4-38)$$

IV.2 Application of Stress Free Formulation

Combining (4-38) and (4-26) gives an expression for total normalized displacement due to a shear wave incident upon a stress free boundary. This expression was implemented on the computer and run for various values of γ_s , using the center frequency of the passband, 2650 Hz, required in the lab. All media parameters used were those of the physical model, allowing for direct comparison of the two results. Fortran 77 code for this case is given in Appendix 2.

IV.3 Numerical Stress Free Results

72° to 90° Angle of Incidence

Normalized displacements were calculated for angles of incidence starting at 72°, which represents the physical model, to perfect grazing. Calculations were carried out to a large distance from the fracture to guarantee steady state conditions were reached. The results are shown in Figures 4-2 to 4-5.

A few simple tests can be applied to these plots to check their validity. First, no amplitude can be greater than two. The incoming wave was set to have unit amplitude, therefore even if perfect reflection and constructive interference occurred an amplitude of two cannot be surpassed. Second, an increase in apparent wavelength with increasing incident angle should be observed. It is obvious that all figures satisfy these criteria.

Comparison of figures (4-2) and (4-3) with (4-4) and (4-5) leads to the conclusion that 72° and 85° do not represent a case of grazing incidence. The amplitude of the displacement at the fracture should be zero or nearly so, if grazing is achieved. The results for 89° and 90° illustrate this phenomenon. It should be noted that for perfect

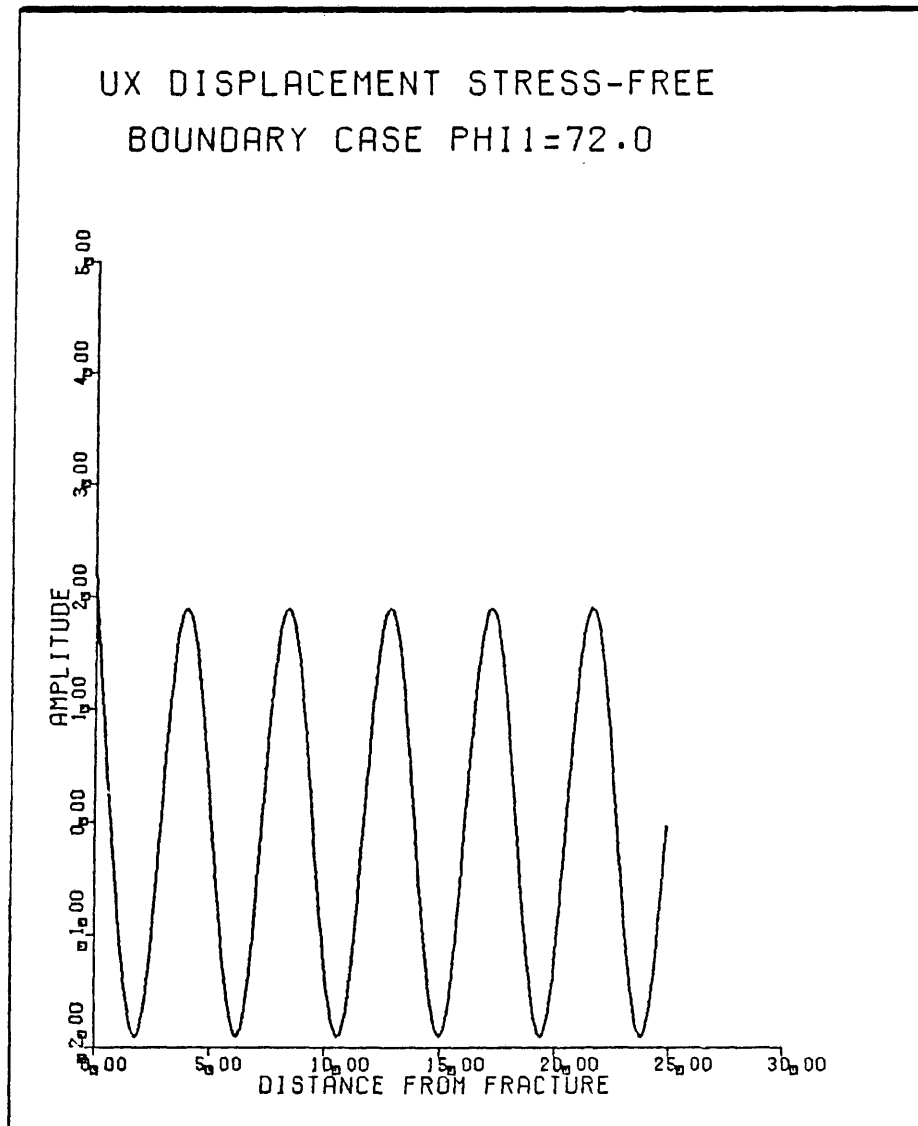


Figure 4-2

Numerical Normalized Displacement Amplitude, Stress
Free Boundary. Angle of Incidence = 72° .

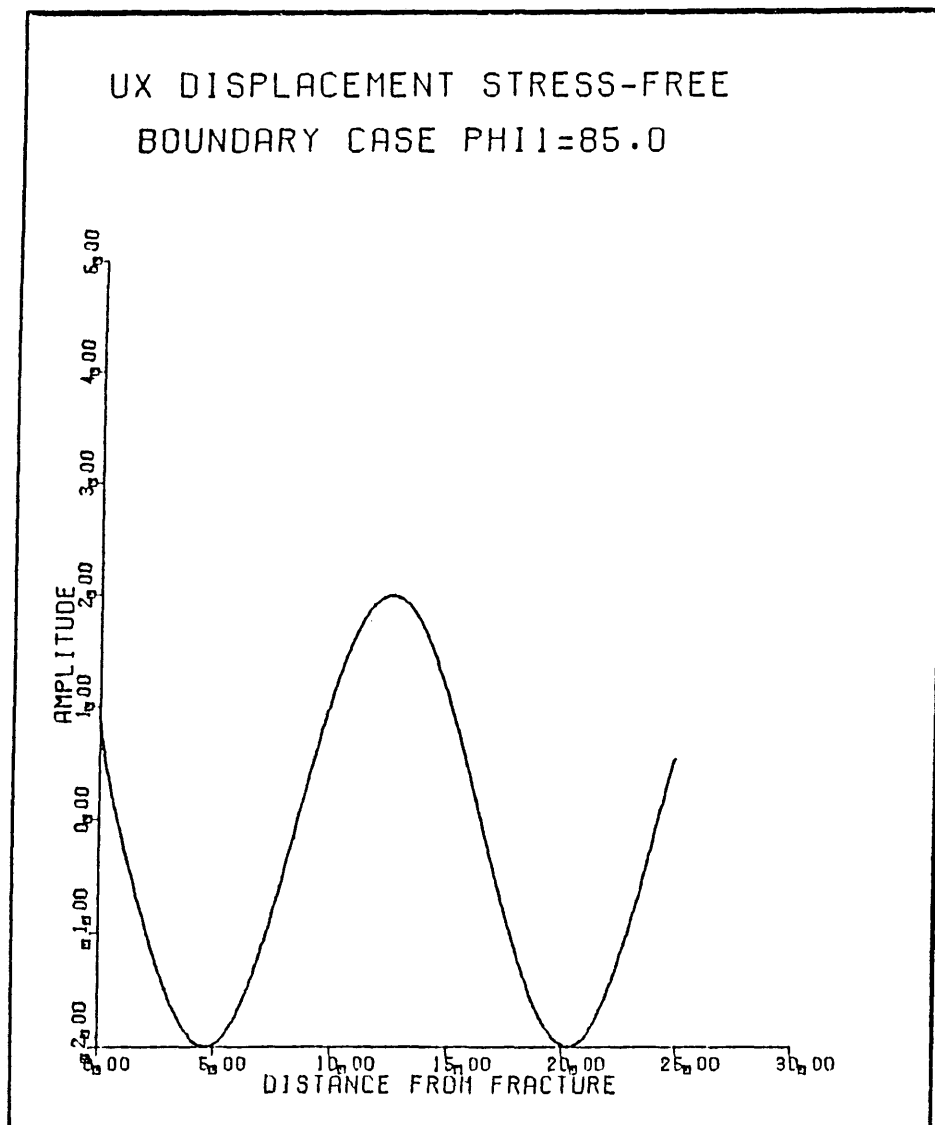


Figure 4-3

Numerical Normalized Displacement Amplitude, Stress
Free Boundary. Angle of Incidence = 85° .

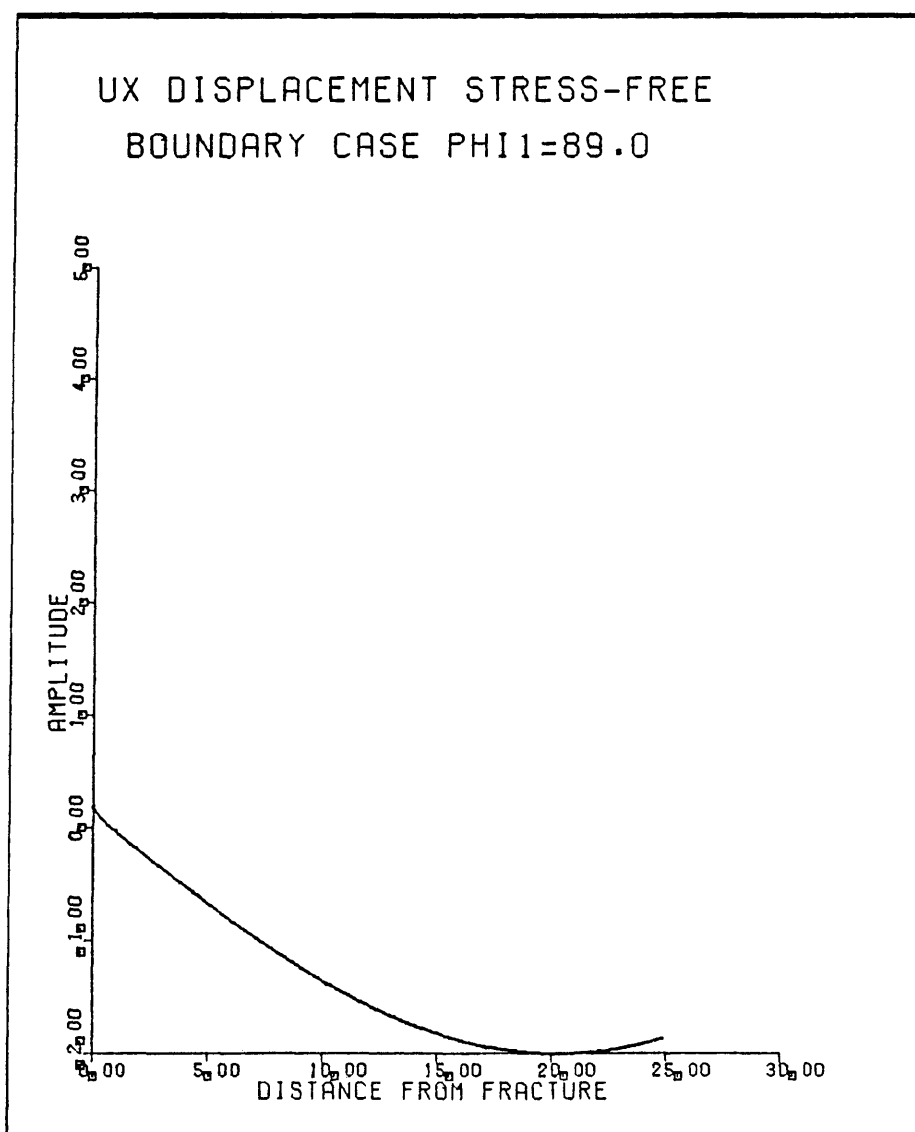


Figure 4-4

Numerical Normalized Displacement Amplitude, Stress
Free Boundary. Angle of Incidence = 89° .

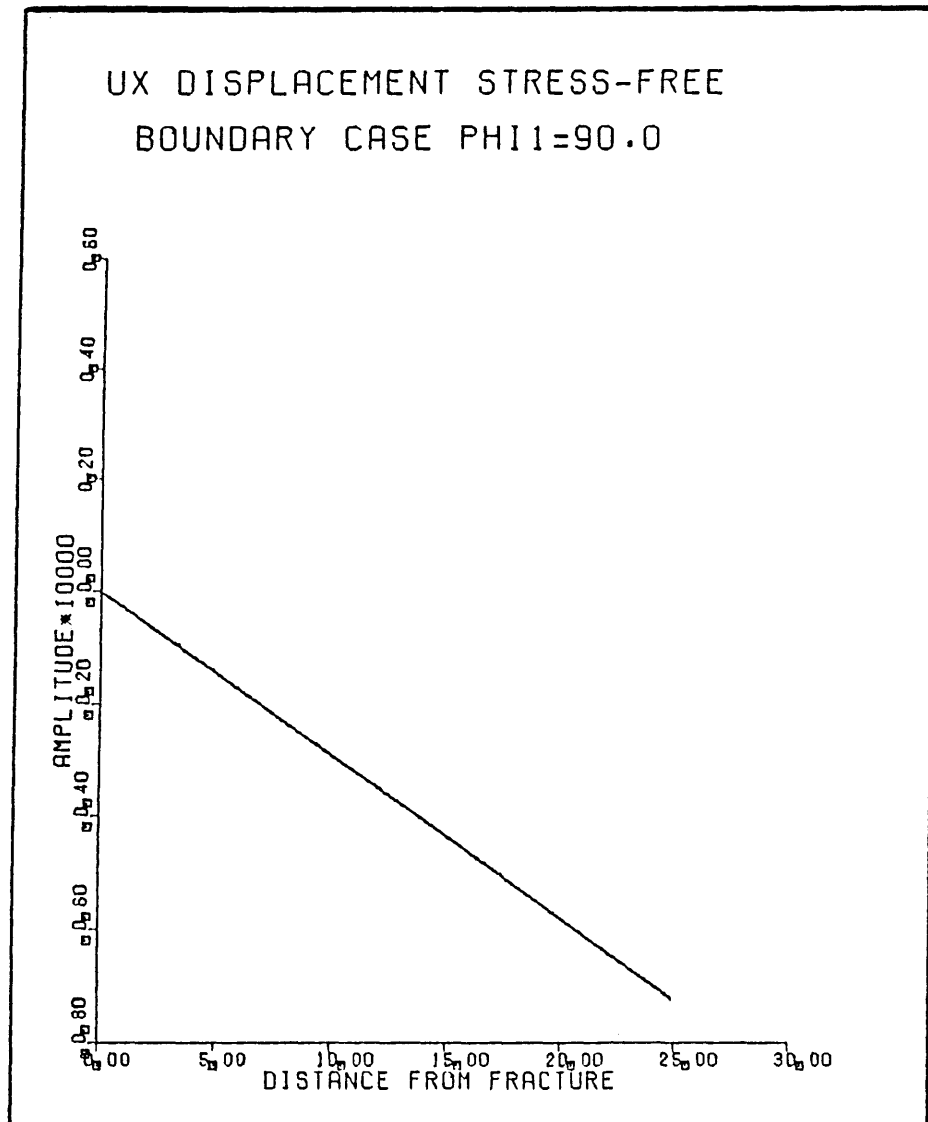


Figure 4-5

Numerical Normalized Displacement Amplitude, Stress

Free Boundary. Angle of Incidence = 90° .

ARTHUR LAKES LIBRARY
COLORADO SCHOOL of MINES
GOLDEN, COLORADO 80401

grazing, 90° , the amplitudes of figure (4-5) have to be scaled by a factor of 10000. Ideally this plot should remain at zero, however, deviation results due to computer rounding error.

Comparison to Physical Experiment

The purpose of numerically investigating the case of reflection from a stress free boundary is twofold. First, a check was required which would allow for the setting of some standard against which the experimental results could be compared and second, we will later compare the stress free case to a more realistic theory.

Figures (4-6) through (4-9) provide the means through which comparison of the two cases is most clear. The experimental curves, represented by the heavier lines, are identical to those presented earlier. Flattening has occurred simply because the vertical axis has been expanded to allow for inclusion of all numerical data. Thin lines represent the theoretical curves which have only been plotted out to 1.0 feet, and have been rectified.

Cursory examination of Figures (4-6) through (4-9) might lead to the conclusion that there is no agreement between the data sets. However, qualitative agreement is evident after more detailed comparison.

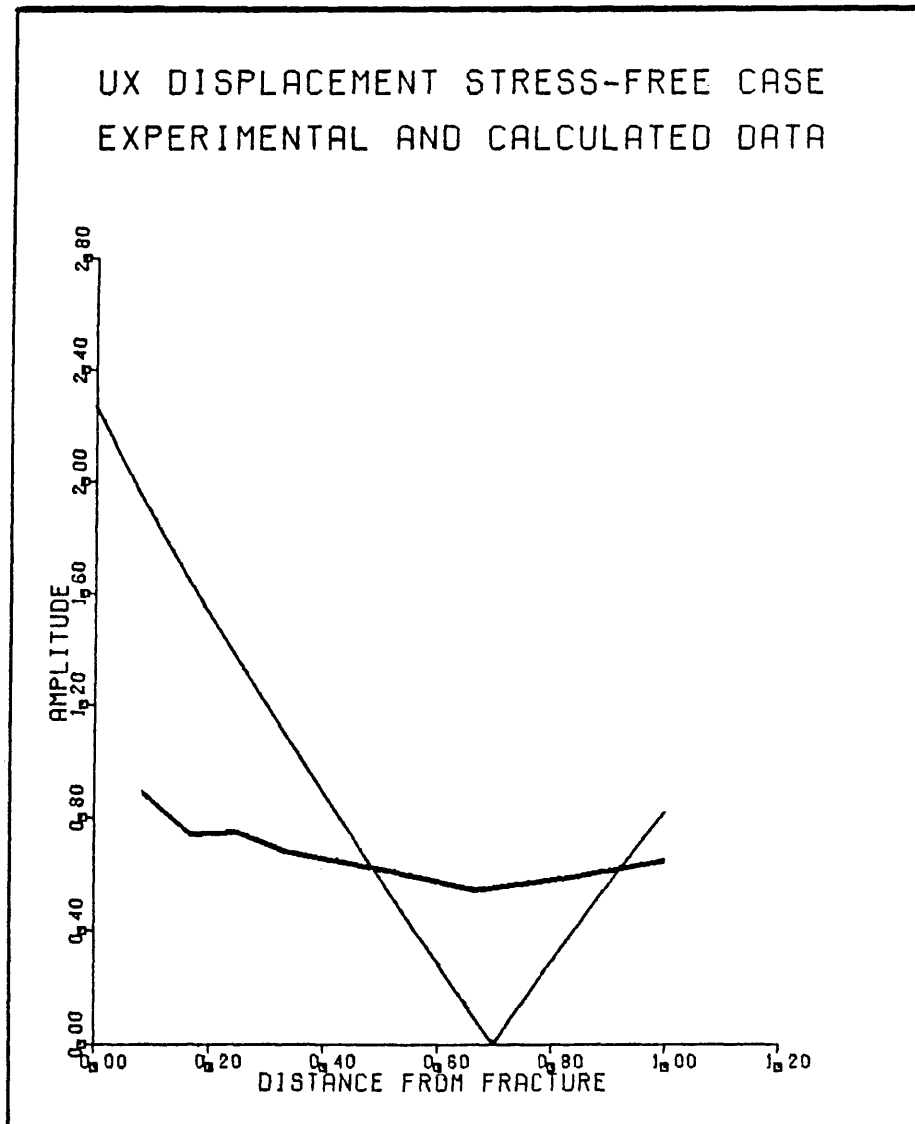


Figure 4-6

Numerical Stress Free Data for Incident Angle of 72°
and Experimental Data at $Y=2$.

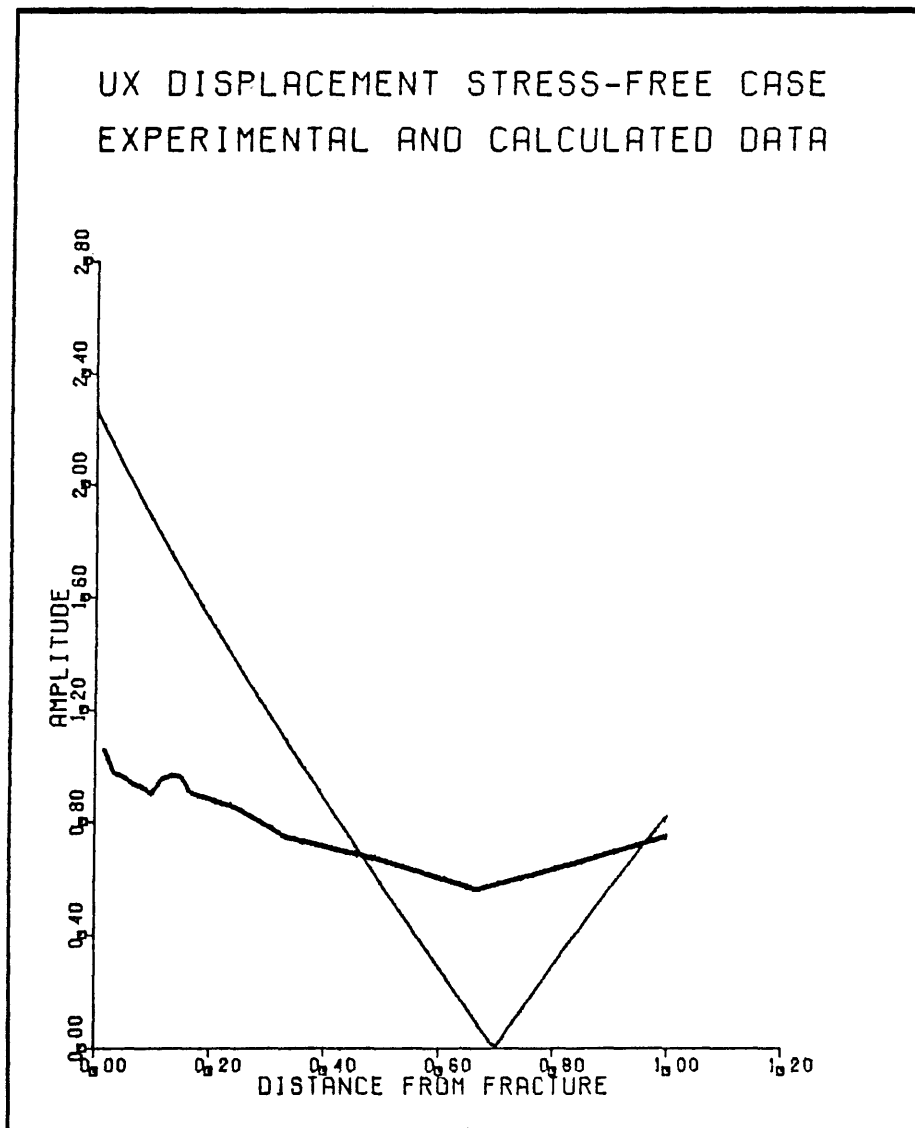


Figure 4-7

Numerical Stress Free Data for Incident Angle of 72°
and Experimental Data at $Y=12$.

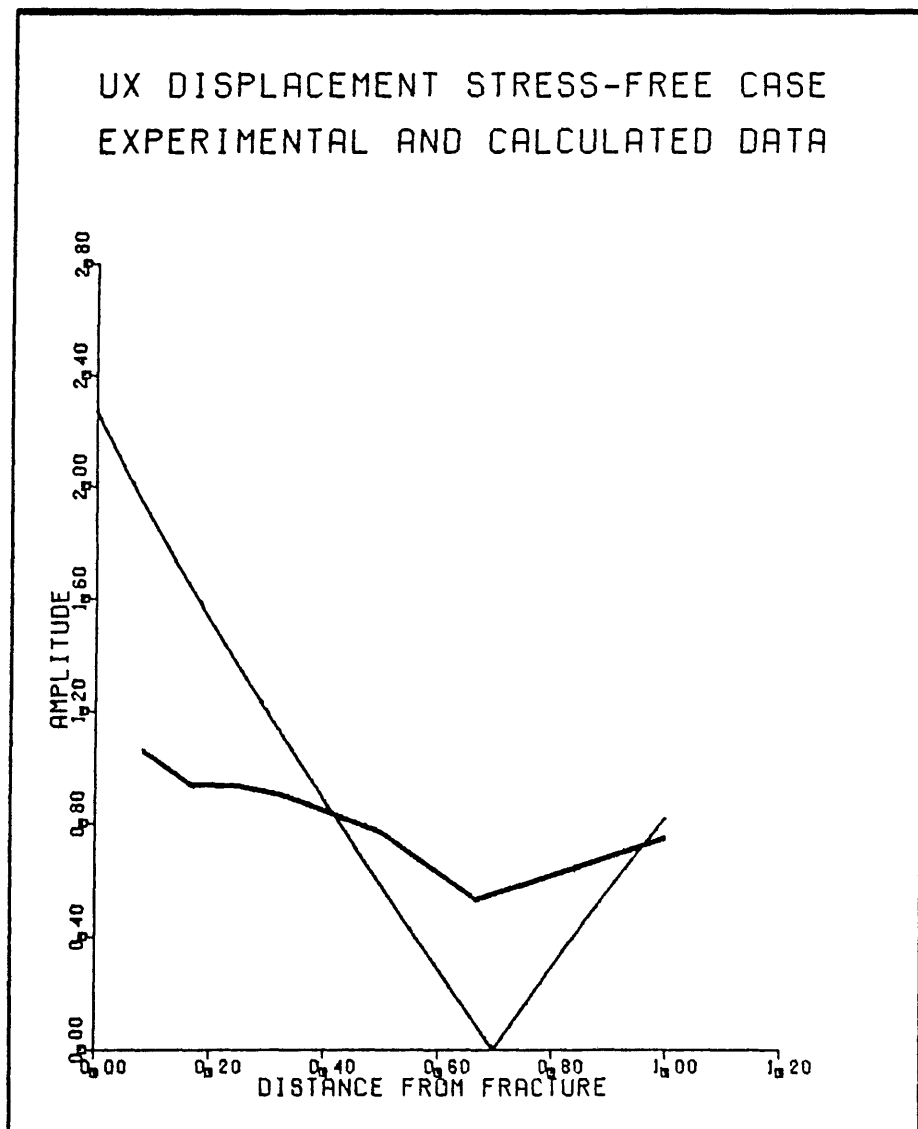


Figure 4-8

Numerical Stress Free Data for Incident Angle of 72°
and Experimental Data at $Y=20$.

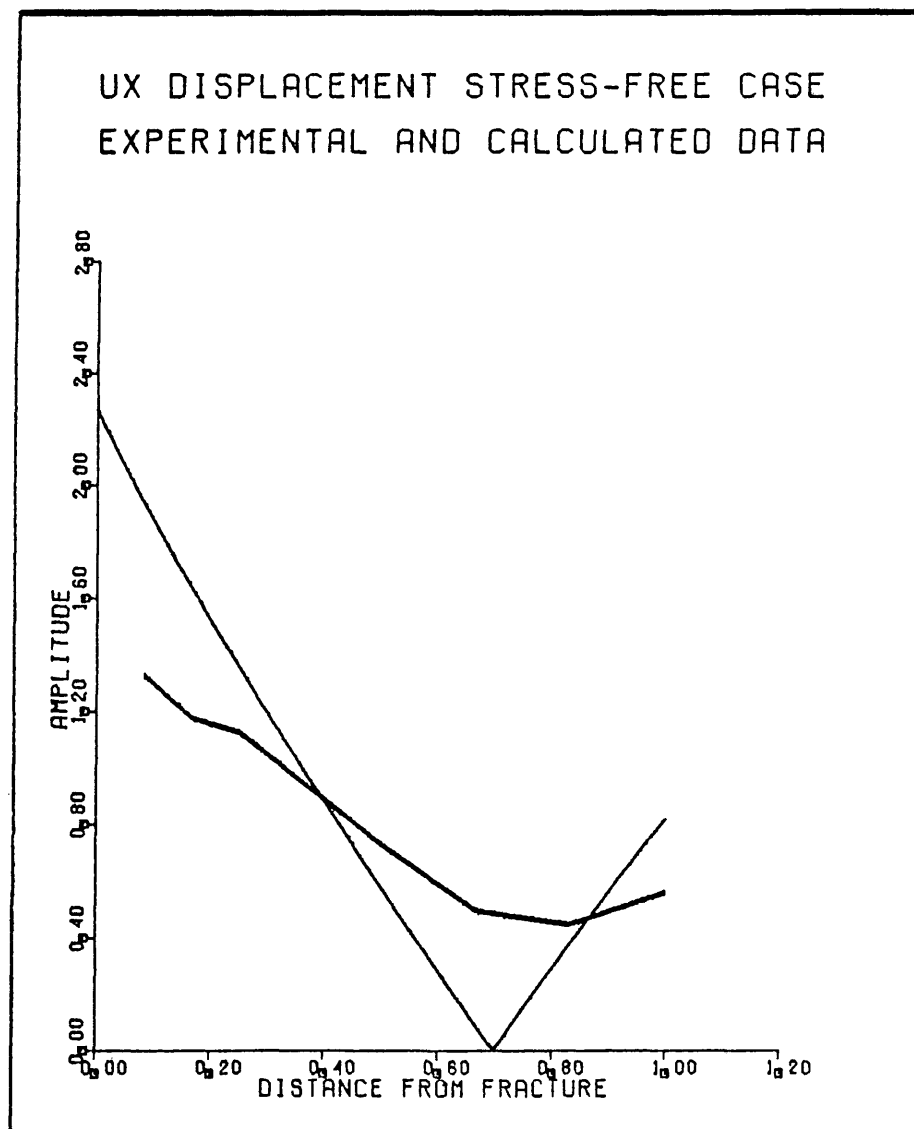


Figure 4-9

Numerical Stress Free Data for Incident Angle of 72°
and Experimental Data at $Y=28$.

The most important characteristic the data sets share is the general trend of the curves, all maxima and minima occur in approximately the same spatial position. This observation leads us to conclude that the empirical data is a rough scaled version of the mathematical.

Differences in the curves are the result of very basic variances in the way each data set was generated. Clearly, any empirical data is expected to be more noisy than a computer generated curve, but the differences go beyond noise. The experimental curves are much more broad and flat. This is primarily due to summation of many frequency components resulting in the waveform which was measured on the scope. In contrast, the numerical curves were generated by considering one frequency, which represented the center of the pass-band used in filtering the recorded waveforms. Compensation for this difference would occur through displacement amplitude calculations and summation for a number of frequencies at each point along the profile. (Refer to figures 5-14 and 5-15 for comparison of computations at different frequencies.)

Diffractions are generated when a wavefield encounters a surface or discontinuity that is small compared to the wavelength of the energy. This occurs in the plexiglas at the beginning of the fracture. Interference by scattered waves can result in amplitude changes of measured first break

energy. Diffraction theory was not incorporated into the mathematical model.

The comparison of these two data sets lead to some interesting conclusions. First, the geometry which was built into the lab model does not allow for examination of the problem in question, at near grazing incidence. The numerical results bear this out. Second, even though the lab model did not achieve its intent, the results that were acquired are confirmed by the mathematical theory indicating that the exercise has some validity.

V. Linear Slip Boundary

Schoenberg (1980) developed theory which investigated elastic wave behavior across a linear slip interface. Such an interface is imperfectly bonded, which is taken to mean that the stress is continuous across the boundary, while the displacement is not. The vector difference in the displacement is assumed to be linearly dependent upon the stress. This condition is termed "linear slip" and replaces the requirement of continuous displacement that represents a perfectly bonded interface.

The linear slip condition is a more realistic model of a buried fracture. In the earth it is not difficult to imagine points of contact along the length of a fracture. This situation is not likely to be modeled well by the stress free case developed earlier, but requires theory to account for this contact.

Our specific problem investigates reflection phenomena resulting from high incidence angles. Schoenberg's (1980) work did not consider angles of incidence beyond the critical angle, which is precisely what grazing or near grazing requires. Therefore we develop our theory from White's (1983) work and incorporate the linear slip through one of the required boundary conditions.

V.1 Mathematical Development

Figure 5-1 illustrates the situation we consider. An interface exists in the yz plane in a uniform medium at $x = 0$. Shear energy is incident upon the boundary with angle γ_s setting up reflected and transmitted wavefields. Potentials can be written describing these fields whose amplitudes can be solved for by imposing the linear slip boundary conditions. The potentials taken from White (1983) equation (2-40), where primed values represented transmitted energy and non-primed represent reflected energy are:

Compressional:

$$\phi = A_2 e^{-\bar{m}x} e^{ilz} e^{i\omega t} \quad (5-1)$$

$$\phi' = A_1' e^{\bar{m}x} e^{ilz} e^{i\omega t} \quad (5-2)$$

Shear:

$$\psi = (B_1 e^{ikx} + B_2 e^{-ikx}) e^{ilz} e^{i\omega t} \quad (5-3)$$

$$\psi' = B_1' e^{ikx} e^{ilz} e^{i\omega t} \quad (5-4)$$

Now the stated boundary conditions require continuity of stress at $x = 0$,

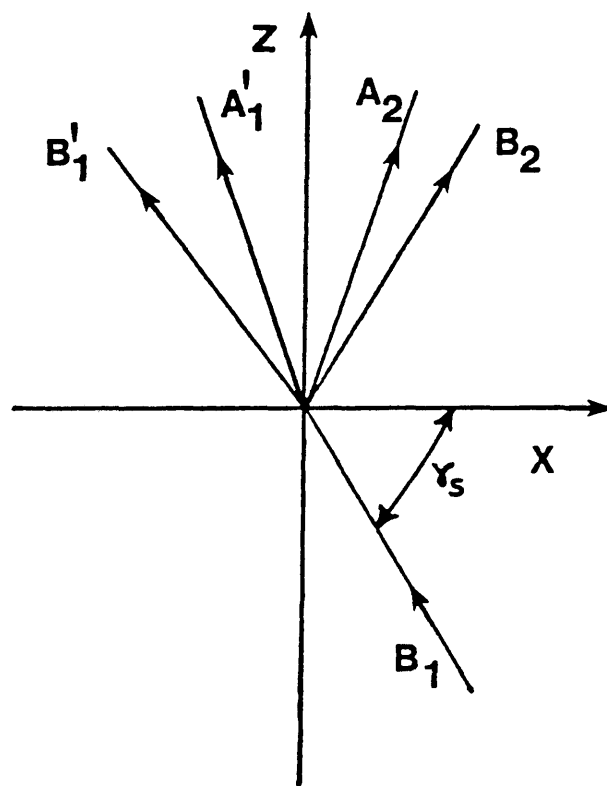


Figure 5-1

Wavefields Studied at Linear Slip Boundary.

$$P_{xx} - P'_{xx} = 0 \quad (5-5)$$

$$P_{zx} - P'_{zx} = 0 \quad (5-6)$$

and for the displacement,

$$U_x - U'_x = 0 \quad (5-7)$$

$$Q(U_z - U'_z) = P_{zx} \quad (5-8)$$

where the second condition satisfies the linear slip requirement. The value Q is what describes the response the fracture has to the wavefield. It can be viewed as the stiffness of the fracture. A very stiff fracture would result in essentially no interface being present, therefore no reflection would occur. On the other hand a much less stiff or very compliant boundary would represent a case where a large amount of energy is reflected.

Imposing the boundary conditions through use of equation (2-22) White (1983) allows construction of a system of four equations in four unknowns, since B_1 , the incoming wave is again set to have unit amplitude. If we express l , k and \bar{m} in terms of γ_s as:

$$l = -w/c = -w \sin \gamma_s / \beta \quad (5-9)$$

$$k = w \cos \gamma_s / \beta \quad (5-10)$$

$$\bar{m} = w (\sin^2 \gamma_s - \beta^2 / \alpha^2)^{1/2} / \beta \quad (5-11)$$

and suppress t dependence, the system of equations is:

$$\begin{vmatrix} a & a & ib & -ib \\ c & -c & -\sin 2\gamma_s & -\sin 2\gamma_s \\ 2iab & 2iab & -c & c \\ 2iab+bd & -bd & d\cos \gamma_s - c & d\cos \gamma_s \end{vmatrix} \cdot \begin{vmatrix} A_2 \\ A_1' \\ B_2 \\ B_1' \end{vmatrix} = \begin{vmatrix} -ib \\ \sin 2\gamma_s \\ c \\ c + d\cos \gamma_s \end{vmatrix} B_1$$

where

$$a = (\sin^2 \gamma_s - \beta^2 / \alpha^2)^{1/2} \quad (5-12)$$

$$b = \sin \gamma_s \quad (5-13)$$

$$c = \cos 2\gamma_s \quad (5-14)$$

$$d = Q_i / \rho w \beta \quad (5-15)$$

Solution of this system by Gaussian elimination gives the values of the amplitude vector. These values can then be used to compute the displacement amplitude resulting from

the incident and reflected wavefields, normal to the fracture. From White (1983) equation (2-22),

$$U_x = \partial\phi/\partial x - \partial\psi/\partial z \quad (5-16)$$

at $x = z = 0$, with time suppressed,

$$U_x = -\bar{m}A_2 - ilB_1 - ilB_2 . \quad (5-17)$$

If \bar{m} and l are again expressed in terms of γ_s , all quantities are known and solution for U_x is possible.

V.2 Application of Linear Slip Formulation

The preceding mathematical expressions were encoded (Appendix 3) and implemented on the digital computer. Parameters used were those of the physical model. Numerical runs were made using the center frequency of the lab pass band, 2650Hz, as in the stress free case. Angles of incidence of 85° and 72° were investigated. A few cases were also run at approximately the 100% corners of the lab bandwidth 265Hz and 5000Hz for comparison.

The stiffness parameter Q , is one value which had to be determined empirically. The question which had to be answered was: how stiff is a stiff fracture or the converse, how stiff is a compliant fracture? The mathematical theory provides the answer. A very stiff fracture is one that does not provide enough of a boundary for reflection to take place, in essence no fracture at all. Mathematically we then expect an amplitude for U_x of one, this being the result of the presence of the incoming wave. A very compliant fracture is exactly opposite. Much of the incident energy is reflected, therefore U_x amplitudes approach two when incident and reflected waves are in phase, dropping to zero when they are 180° out of phase.

Many values of Q were used to empirically answer the questions stated above. The plots presented in the next

section illustrate the change in waveform amplitude with Q for a given incidence angle. From these results we are able to determine what value of Q is indeed stiff or compliant for this specific case.

V.3 Linear Slip Results

Figures 5-2 through 5-7 illustrate numerical results obtained from application of the linear slip theory to a model with 72° angle of incidence. This directly simulates the geometry of the lab experiment. These plots were generated by using the middle frequency of the lab pass-band, 2650Hz, and have been rectified. The stiffness, Q , was varied over a wide range, providing some interesting results.

Grazing incidence is again not modeled well by 72° . The amplitudes on all the plots are large enough at the boundary to conclude this. Therefore we have agreement between all three cases, lab, stress free, and linear slip, on this point.

The most interesting comparison is between individual curves of this set. Comparing these curves with each other allows for noting the change in wavefield amplitude with Q . Q , the stiffness, was varied by 11 orders of magnitude in creating these plots. Over this range we go from very stiff, resulting in almost no reflection, to extremely compliant, resulting in almost complete reflection.

Comparison of Figures 5-2 and 5-3 demonstrate that the limit of high compliance has been reached. A change of five orders of magnitude has produced almost no change at all in the curves.

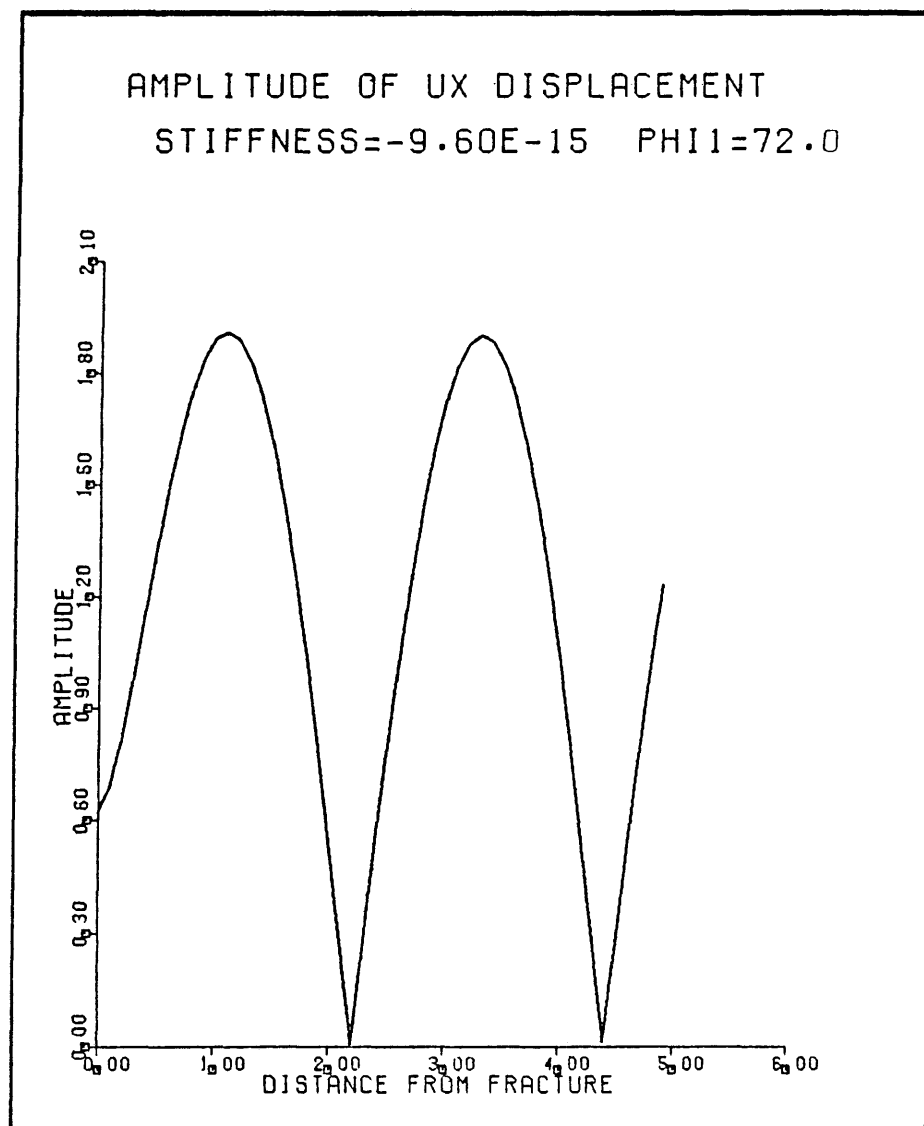


Figure 5-2

Numerical Linear Slip Data, $f=2650\text{Hz}$.

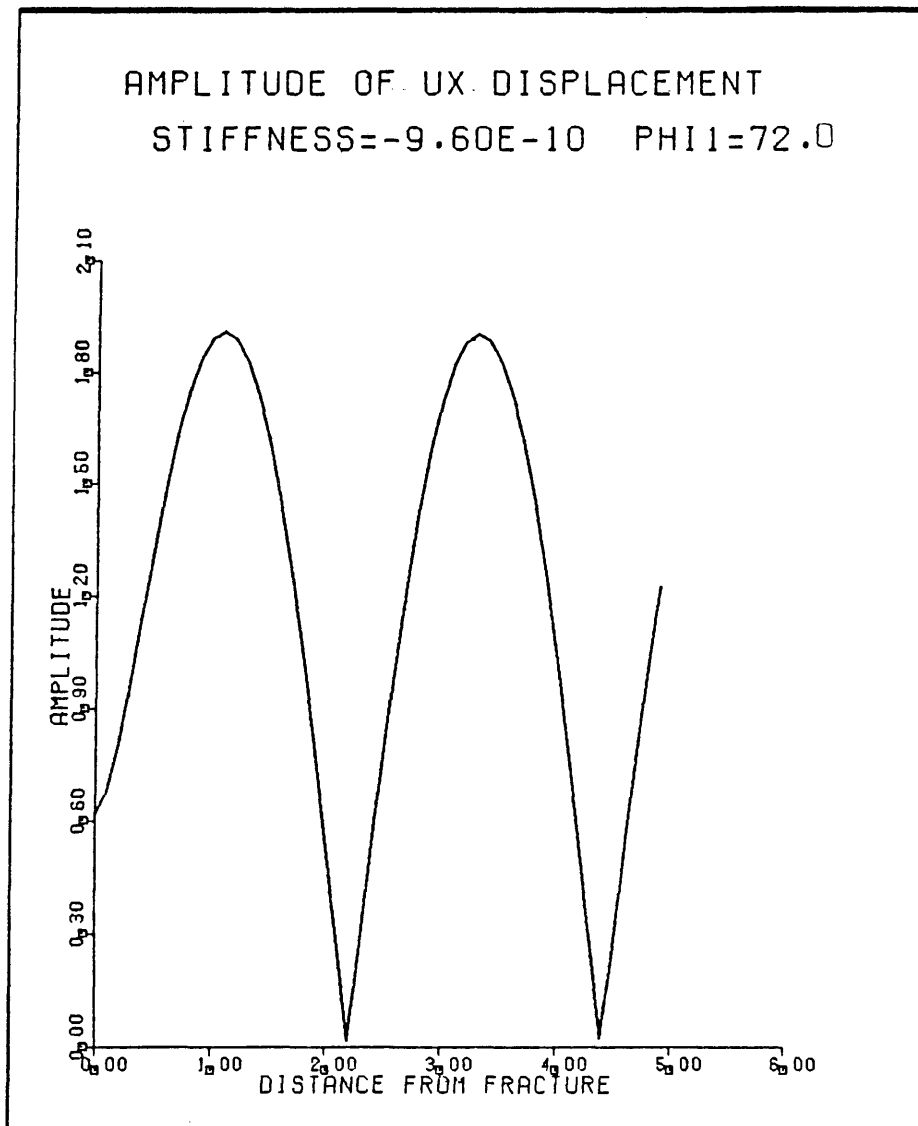


Figure 5-3

Numerical Linear Slip Data, $f=2650\text{Hz}$.

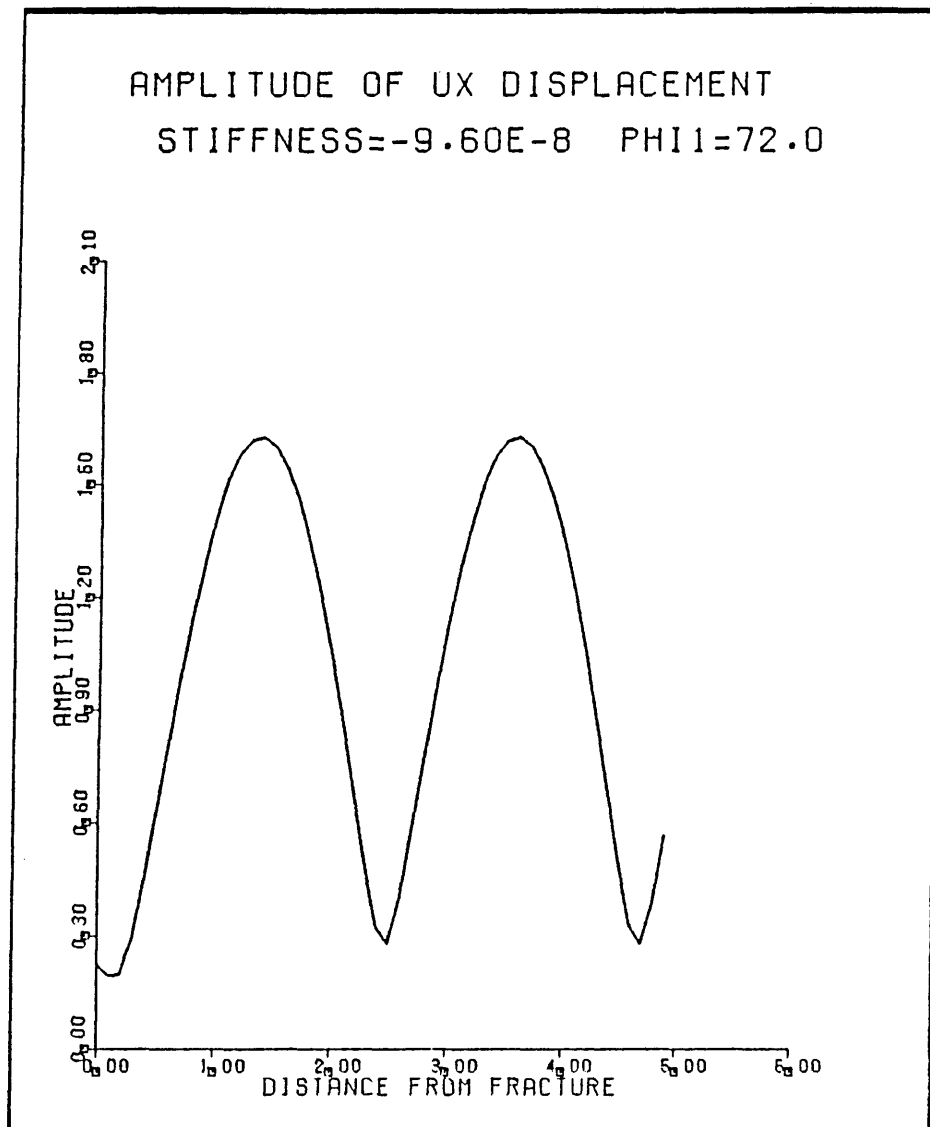


Figure 5-4

Numerical Linear Slip Data, $f=2650\text{Hz}$.

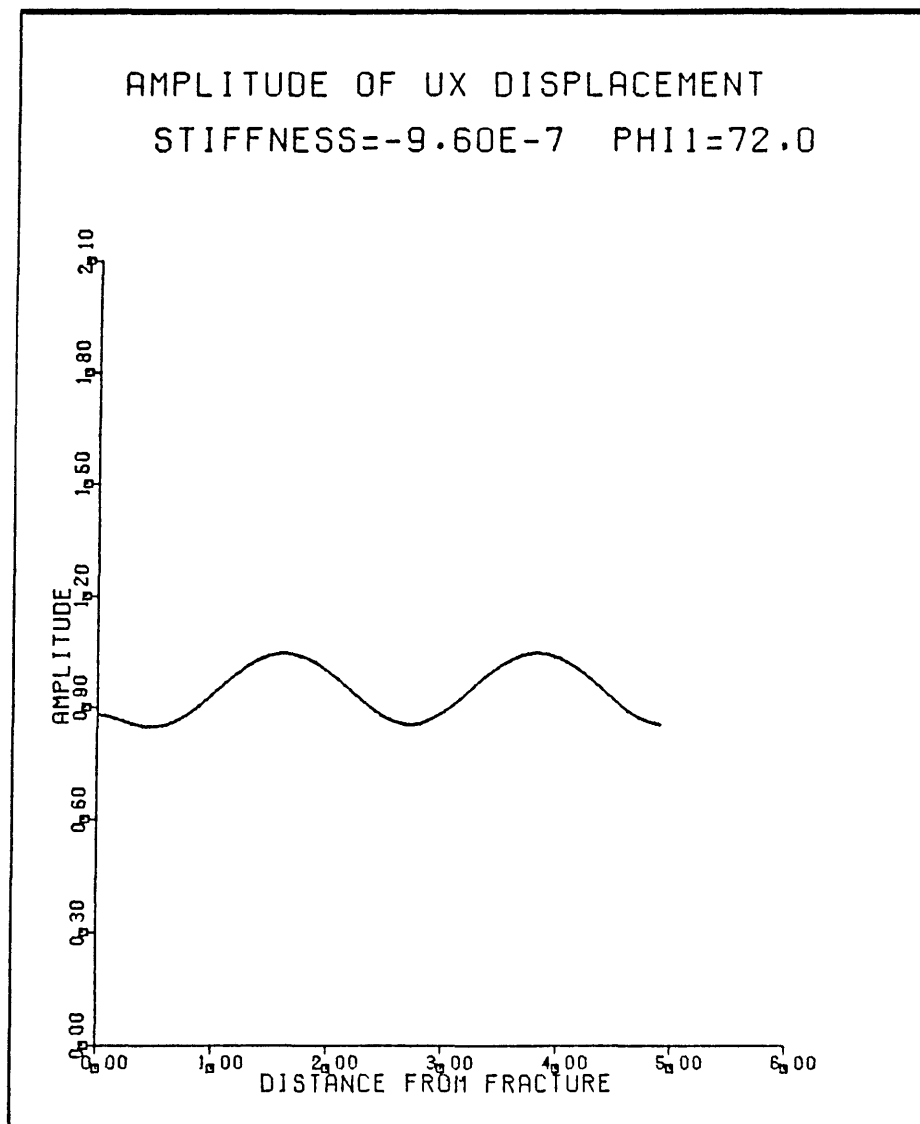


Figure 5-5

Numerical Linear Slip Data, $f=2650\text{Hz}$.

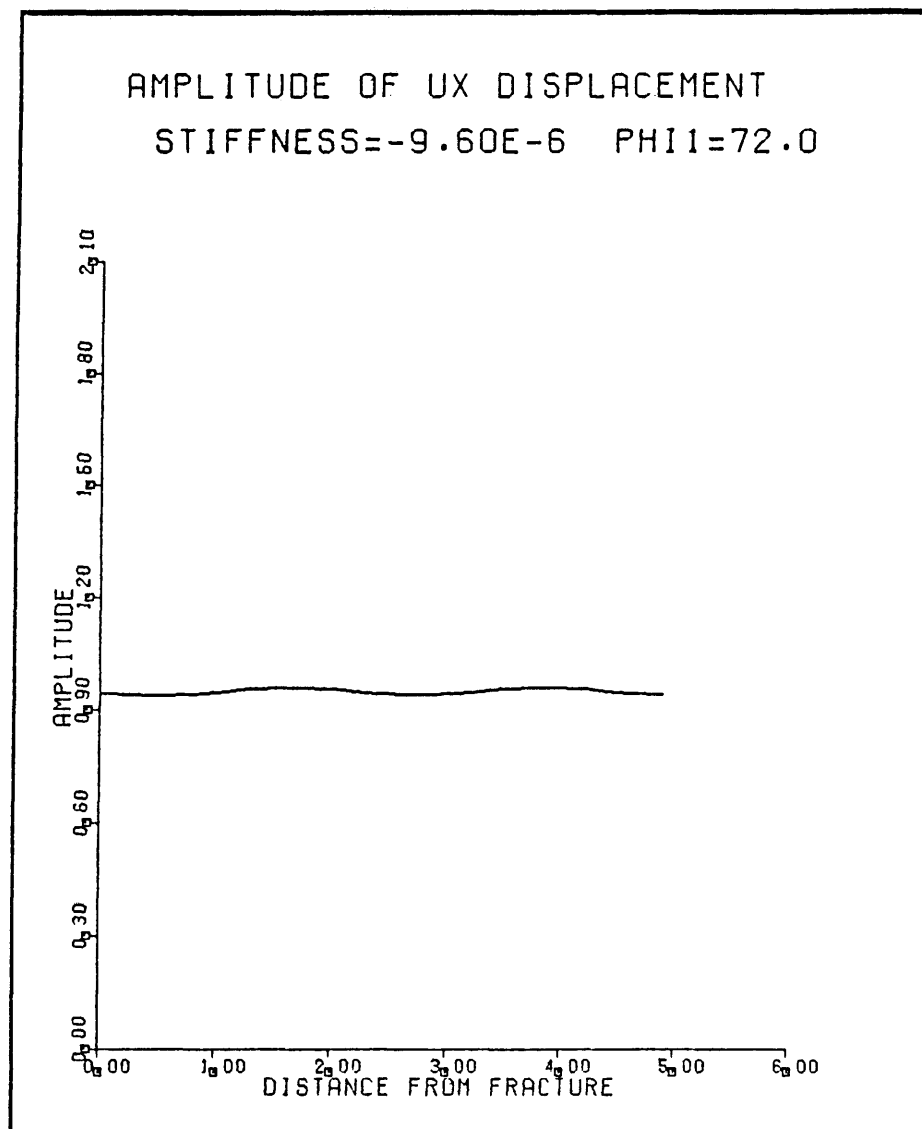


Figure 5-6

Numerical Linear Slip Data, $f=2650\text{Hz}$.

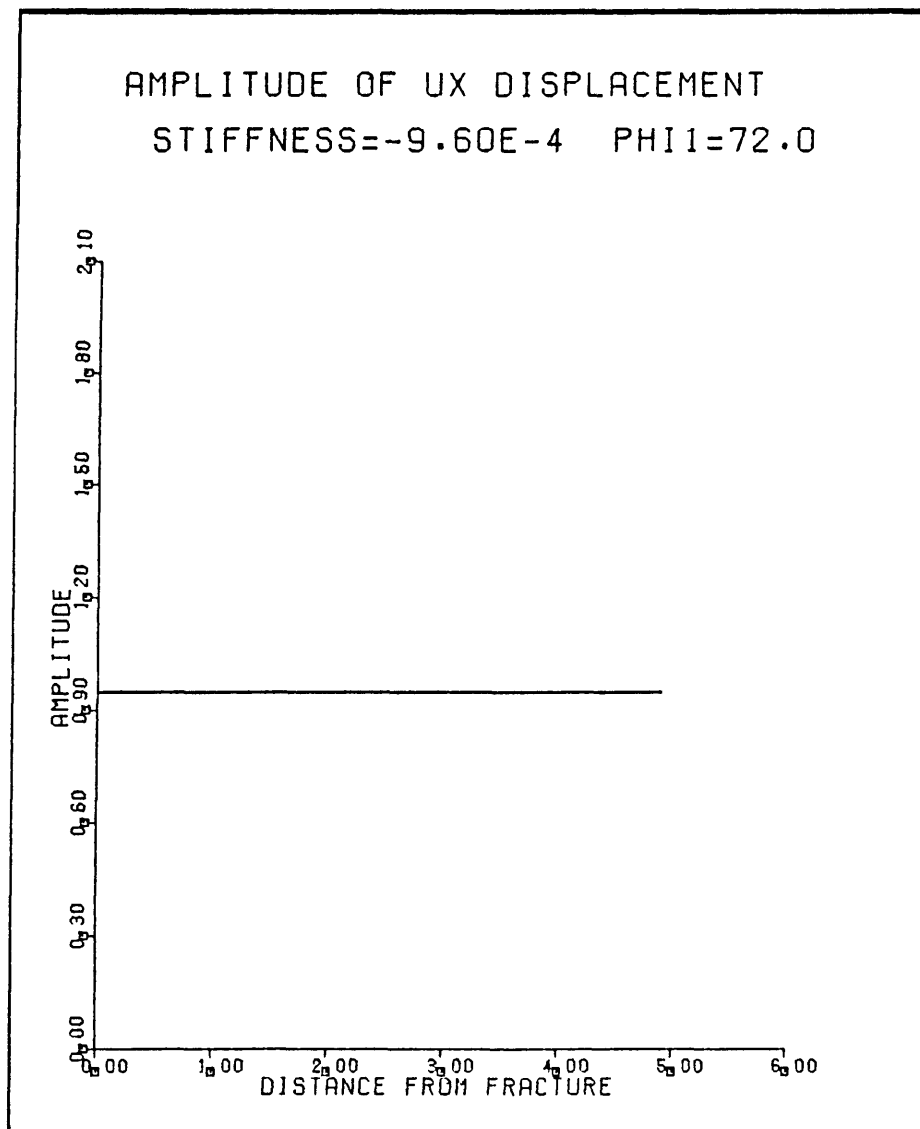


Figure 5-7

Numerical Linear Slip Data, $f=2650\text{Hz}$.

These two runs would represent the case of a very compliant fracture, amplitudes approach two where reflected and incident energy are in phase, and drop to zero when out of phase. Note that although Figure 5-3 does not appear to go completely to zero this is due to spatial sampling density, not waveform amplitude.

In moving from Figure 5-3 to 5-7 the increase in stiffness is seen to reduce displacement amplitude. As Q increases more energy is transmitted through the interface, than reflected. Figure 5-7 represents a situation where the fracture is so stiff it really provides no interface at all and reflection does not take place. The calculated displacement is then equal to one and is the result of the presence of the incoming wave. Figures 5-3 and 5-7 allow for determination of what Q value represents a stiff or compliant fracture for this model.

Figures 5-8 through 5-13 are identical to the previous set of plots with the exception that the incident angle has been changed to 85° . In addition to the obvious change in apparent wavelength, we should also expect some amplitude reduction at the interface for a very compliant fracture as 85° is closer to grazing than is 72° . Comparison of Figures 5-8 with 5-2 confirms this phenomenon.

Figures 5-14 and 5-15 were created to illustrate the effect of a change in incident wavefield frequency. Both

plots were created using 72° as an incident angle and a Q which represents high compliance. As expected, both runs result in significant amplitude at the boundary and differ only in the wavelength of the energy. Again note that Figure 5-15 should should go to zero, but spatial sampling was insufficient to illustrate this.

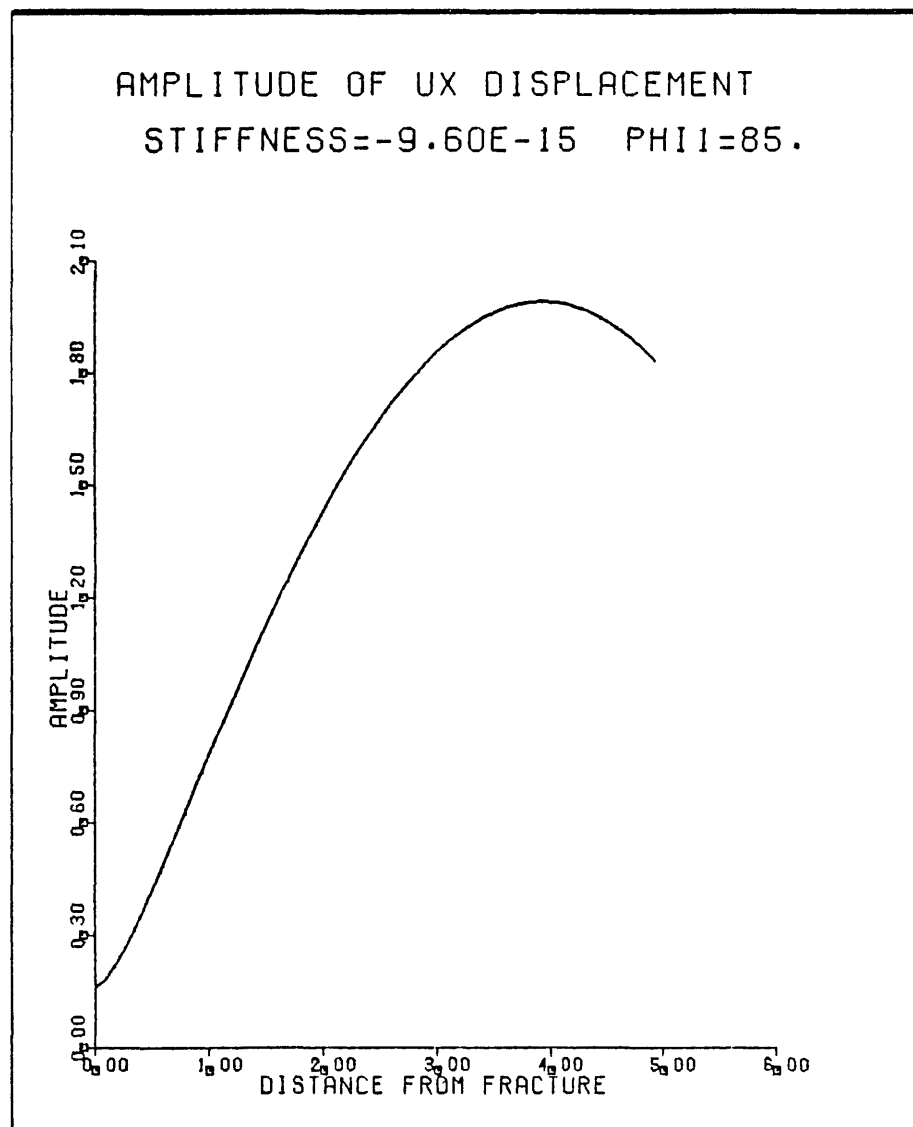


Figure 5-8

Numerical Linear Slip Data, $f=2650\text{Hz}$.

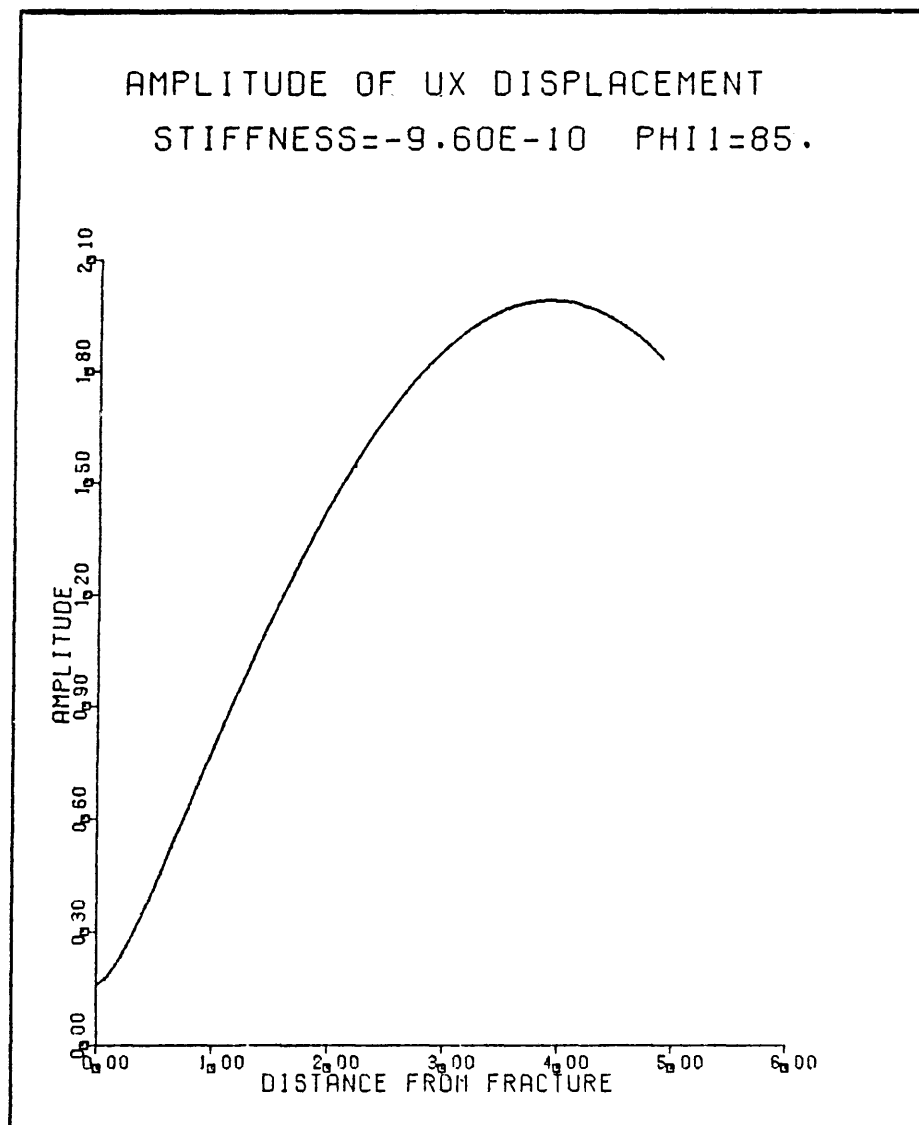


Figure 5-9

Numerical Linear Slip Data, $f=2650\text{Hz}$.

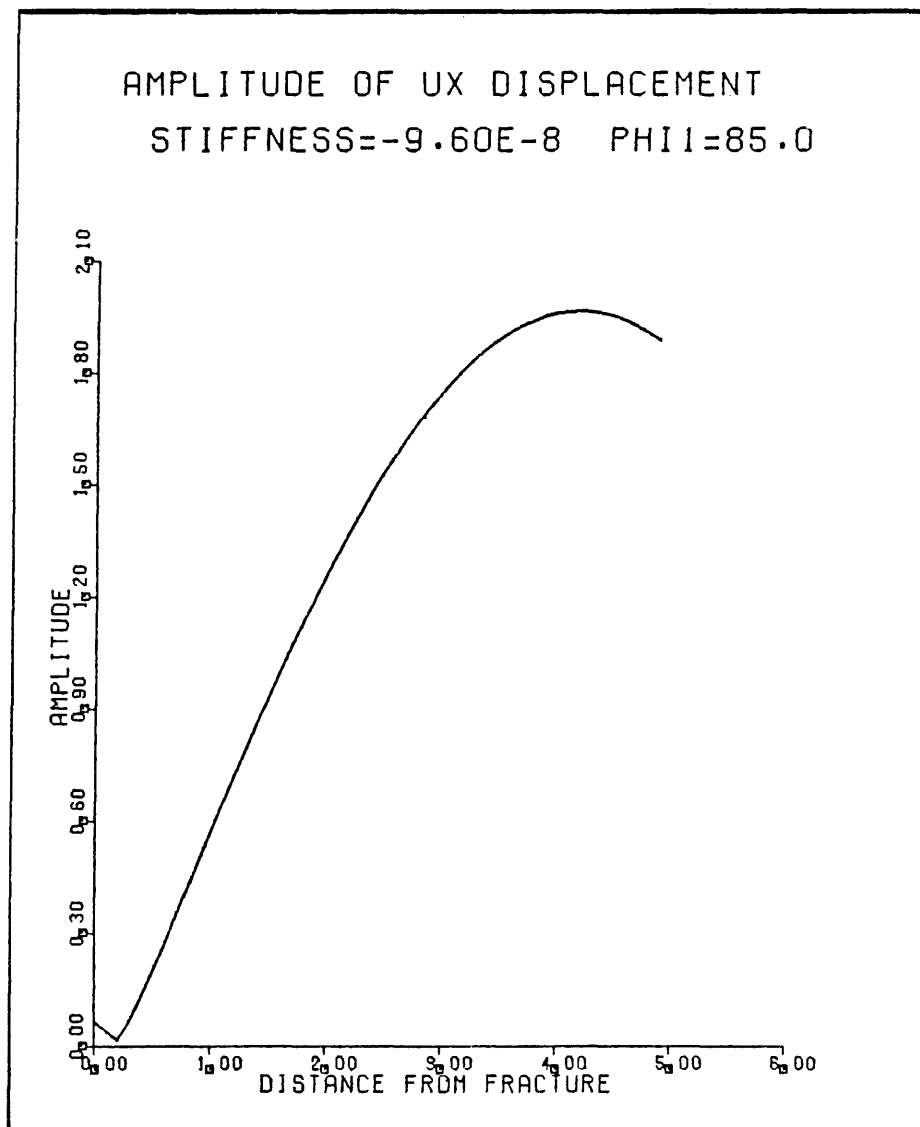


Figure 5-10

Numerical Linear Slip Data, $f=2650\text{Hz}$.

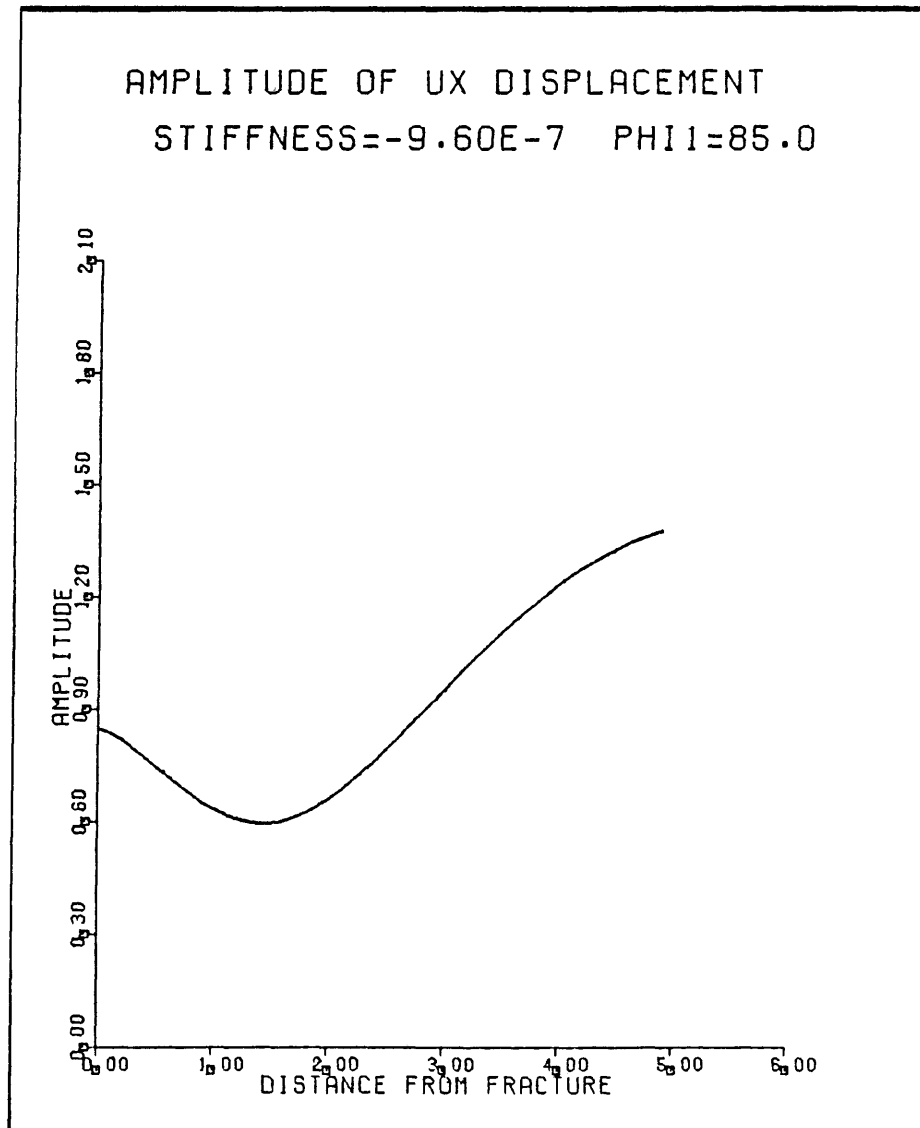


Figure 5-11

Numerical Linear Slip Data, $f=2650\text{Hz}$.

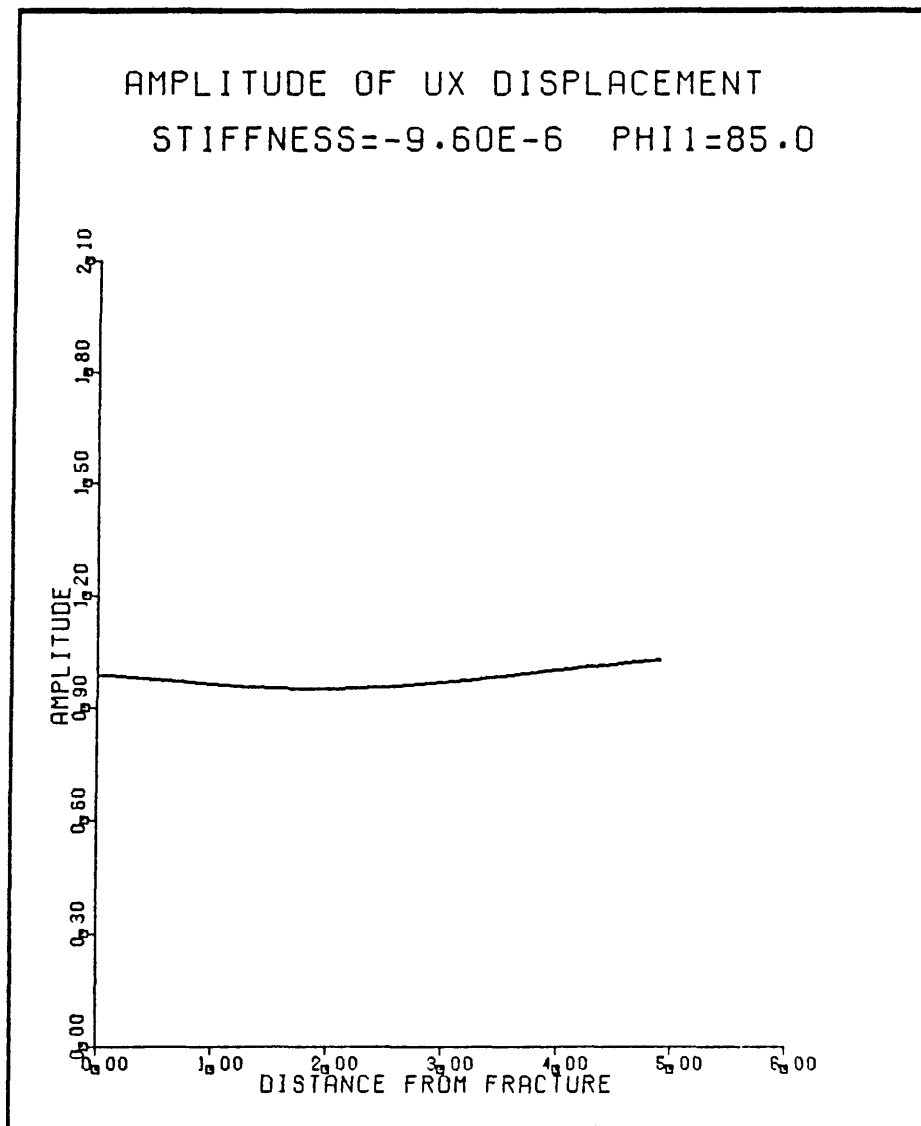


Figure 5-12

Numerical Linear Slip Data, $f=2650\text{Hz}$.

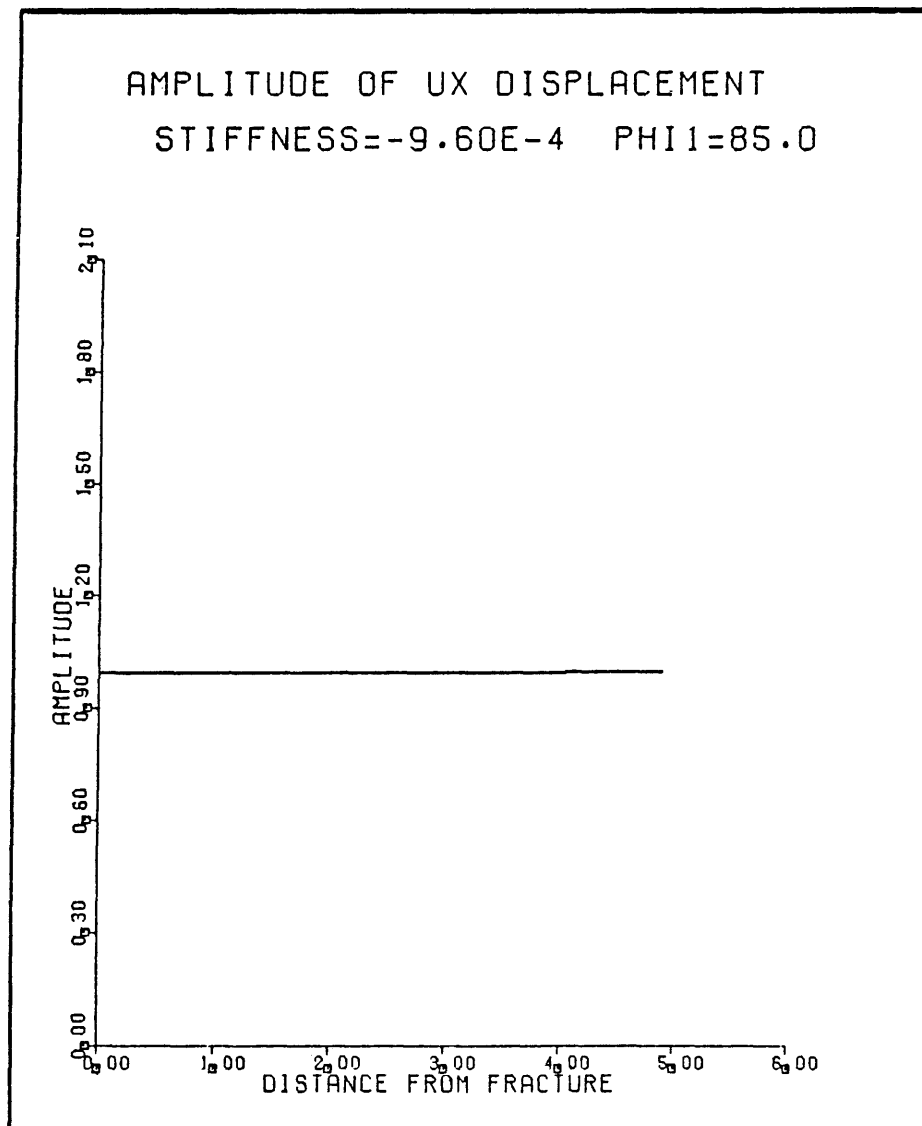


Figure 5-13

Numerical Linear Slip Data, $f=2650\text{Hz}$.

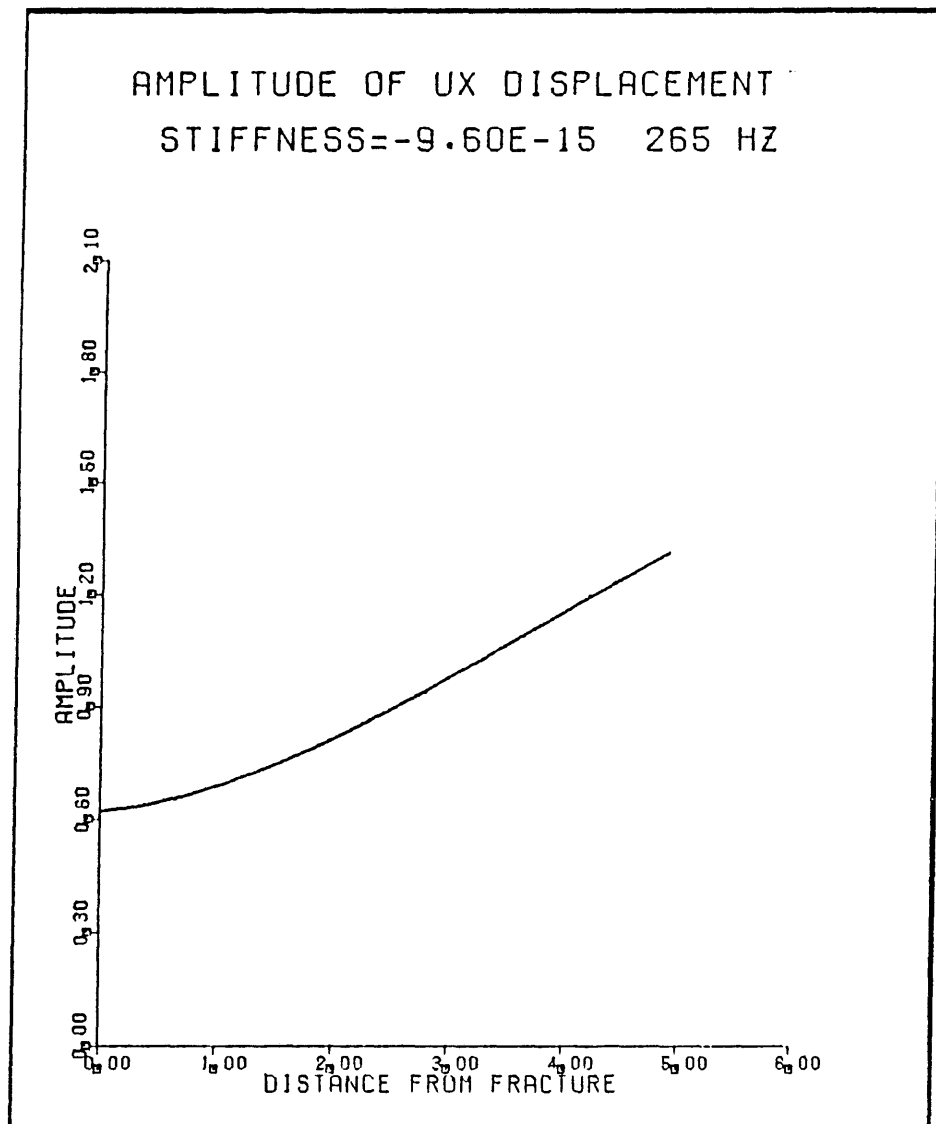


Figure 5-14
Numerical Linear Slip Data, $f=265\text{Hz}$,
Incident Angle of 72° .

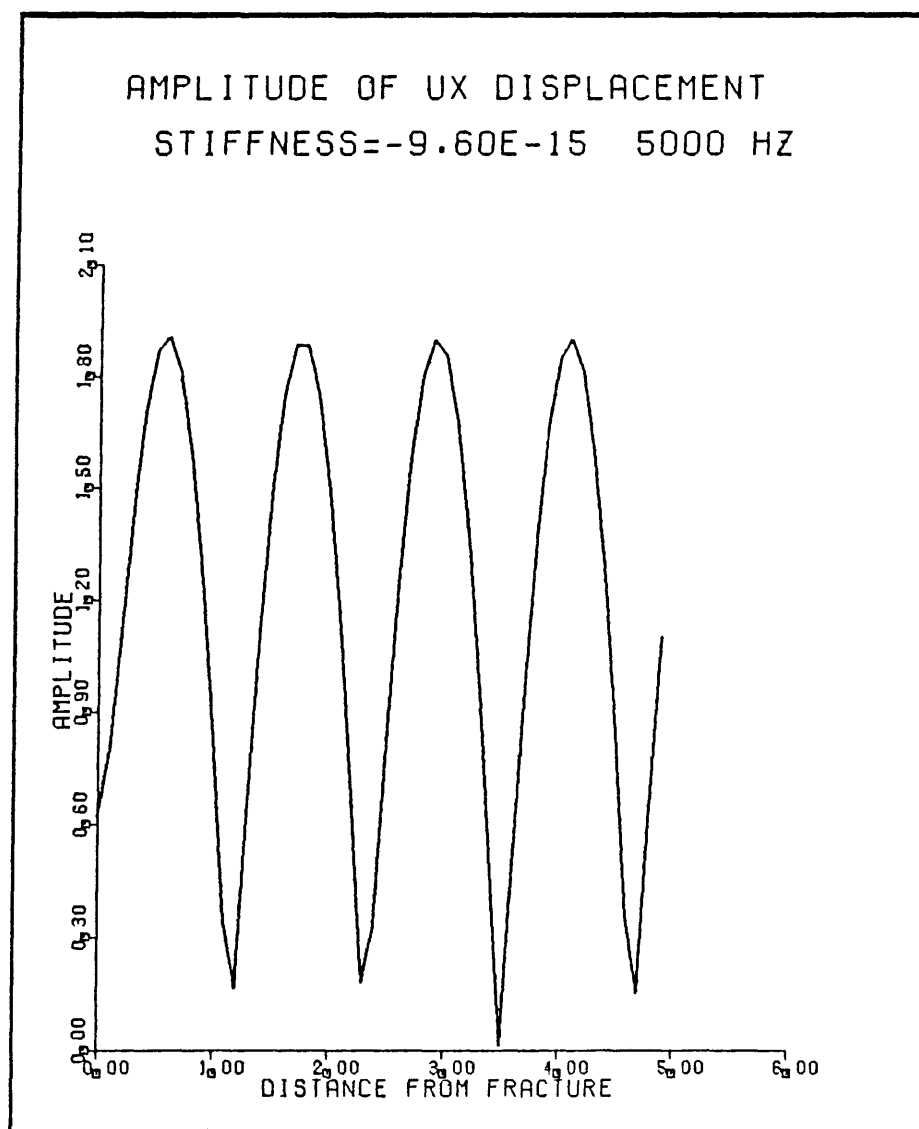


Figure 5-15
Numerical Linear Slip Data, $f=5000\text{Hz}$,
Incident Angle of 72° .

VI. Conclusions

In this study we have attempted to demonstrate that an amplitude anomaly is induced upon a reflected SV wavefield by a fracture zone. From the empirical and theoretical work done we can conclude that:

- 1) Lab model geometry did not actually allow for investigation of grazing incidence case.
- 2) From mathematical treatment of stress free boundary, we see that at the boundary the amplitude is totally a function of incident angle.
- 3) The major difference between the numerical stress free results and empirical lab results is due to the number of frequency components contributing to the individual curves.
- 4) Numerical results indicate that in order to see amplitude reduction at fracture interface, the fracture must be very compliant and incident angle must be within 1° - 2° of true grazing.

- 5) Linear slip theory allows characterization of a fracture through the use of the stiffness value Q .
- 6) For the model parameters and geometry used in this study a value of $Q = -9.60 \times 10^{-10}$ represents a very compliant fracture and $Q = -9.60 \times 10^{-4}$ represents a very stiff fracture.
- 7) The stiffness parameter Q is independent of the incident angle.

References

Aki, K., Fehler, M., Aamodt, R., Albright, J., Potter, R., Pearson, C., and Tester, J., 1982, Interpretation of seismic data from hydraulic fracturing experiments at the Fenton Hill, New Mexico, Hot Dry Rock geothermal site: Journal of Geophysical Research, V. 87, pp. 936-944.

Beydoun, W., Cheng, C., and Toksöz, M., 1985, Detection of open fractures with vertical seismic profiling: Journal of Geophysical Research, V. 90, pp. 4557-4566.

Cheng, C., Toksöz, M., and Willis, M., 1982, Determination of in-situ attenuation from full waveform acoustic logs, Journal of Geophysical Research, V. 87, pp. 5477-5484.

Crampin, S., 1985, Evaluation of anisotropy by shear-wave splitting, Geophysics, V. 50, pp. 142-152.

Fehler, M., Turpening, R., Blackway, C., and Mellen, M., 1982, Detection of a hydrofrac with shear wave vertical seismic profiles, Geophysics, V. 48, pp. 435-436.

Hilterman, F., 1975, Amplitudes of seismic waves - a quick look, Geophysics, V. 40, pp. 745-762.

ARTHUR LAKES LIBRARY
COLORADO SCHOOL of MINES
GOLDEN, COLORADO 80401

Leary, P., and Henyey, T., 1985, Anisotropy and fracture zones about a geothermal well from P-wave velocity profiles, *Geophysics*, V. 50, pp. 25-36.

Paillet, F., and White, J., 1982, Acoustic modes of propagation in the borehole and their relationship to rock properties, *Geophysics*, V. 47, pp. 1215-1228.

Schoenberg, M., 1980, Elastic wave behavior across linear slip interfaces, *Journal of the Acoustical Society of America*, V. 68, pp. 1516-1521.

Trorey, A., 1970, A simple theory for seismic diffractions, *Geophysics*, V. 35, pp. 762-784.

Van der Hijden, J., and Neerhoff, F., 1984, Diffraction of elastic waves by a sub-surface crack (in-plane motion), *Journal of the Acoustical Society of America*, V. 75, pp. 1694-1704.

White, J., 1983, *Underground sound - application of seismic waves*, New York, Elsevier Science.

APPENDIX 1

Electronic Components and Final Settings

Kenwood Stereo Amplifier

Full Gain

Nicolet Digital Oscilloscope

1 microsecond time per point

(±1v) x 1 sensitivity

Trigger - Normal, Act., External

Vertical Expansion x 64

SKL 302 Dual Electronic filter

Filter 1 (low pass)

(x1K) (x5)

Filter 2 (high pass)

(x100) (x3)

Pulse Generator

Trigger Mode Internal

Int. Rep. Rate (.01 - .1)

Pulse Position (0-1), Vernier (10)

Pulse Delay

Pulse Width (1k-10k), Vernier (10)

Pulse Amplitude (100), Vernier (Full)

Pulse Output (-)

Trigger Output (-)

APPENDIX 2

Fortran Code of Program "SFB"

```

* * * * *
C
C   THIS PROGRAM WILL COMPUTE THE AMPLITUDE
C
C   OF THE PARTICLE DISPLACEMENT NORMAL TO
C
C   A STRESS FREE BOUNDARY DUE TO A
C
C   SHEAR WAVE INCIDENT AT AN ARBITRARY
C
C   ANGLE UPON THE BOUNDARY.
C
C   WRITTEN BY RICHARD G. WEBER, AUGUST
C
C   1986
C * * * * *

C   VARIABLE DECLARATIONS AND DEFINITIONS
C
C   SPEED OF COMPRESSIONAL WAVES IN MEDIUM
      REAL ALPHA
C
C   SPEED OF SHEAR WAVES IN MEDIUM
      REAL BETA
C
C   INCIDENT ANGLE OF INCOMING SHEAR WAVE
      REAL PHI1
C
C   FREQUENCY OF INCOMING SHEAR WAVE
      REAL  $\omega$ 
C
C   SPATIAL POSITION WHERE DISPLACEMENT IS CALCULATED
      REAL X
C
C   SHEAR WAVE CONTRIBUTION OF DISPLACEMENT
      REAL Uxs
C
C   COMPRESSIONAL WAVE CONTRIBUTION OF DISPLACEMENT

```

```
      REAL Uxc
C     TOTAL DISPLACEMENT AMPLITUDE NORMAL TO STRESS
      FREE BOUNDARY
      REAL Ux
C     PHASE ANGLE OF INCOMING SHEAR WAVE
      REAL PHZ
C     ALL COMPUTATIONS ARE AT Z=0
C     MODEL PARAMETERS
      ALPHA = 8793.0
      BETA = 3608.0
      PHI1 = 72.0 * 3.14159265/180.0
      w = 2.0 * 3.14159265 * 2650
C     COMPUTATION OF REQUIRED CONSTANTS
      Z1 = BETA**2/ALPHA**2
      Z = SIN(PHI1)**2
      A = ((1./Z)-2. )**2
      B = 4.*SQRT(1.-(Z1/Z))*SQRT((1./Z)-1.)
      PHZ = ATAN(B/A)
      BX = BETA/COS(PHI1)
      D = ABS(4.*SQRT((1./Z)-1.)*((1./Z)-2.))
      E = D/SQRT(A**2+B**2)
C     NOW COMPUTE DISPLACEMENTS FOR A GIVEN X
      DO 5 X = 0.0, 1.00, .01
C     DISPLACEMENT DUE TO SHEAR WAVES
      Uxs = -2.*SIN(PHI1)*SIN((w*X/BX)-PHZ)
```

```
C    DISPLACEMENT DUE TO COMPRESSIONAL WAVES
      Uxc = E*SQRT(Z-Z1)*EXP(-w*SQRT(Z-Z1)**/BETA)
C    NOW COMPUTE TOTAL DISPLACEMENT
      Ux = ABS(Uxs+Uxc)
      WRITE(10,*) X, Ux
5    CONTINUE
      END
```

APPENDIX 3

Fortran Code of Program "LSLP"

```

* * * * *
C
C   THIS PROGRAM COMPUTES PARTICLE DISPLACEMENT
C
C   AMPLITUDES DUE TO A SHEAR WAVE INCIDENT
C
C   UPON A LINEAR SLIP INTERFACE IN A
C
C   SINGLE MEDIUM.  THE PROGRAM TAKES
C
C   REFLECTION, TRANSMISSION AND MODE
C
C   CONVERSION EFFECTS INTO ACCOUNT AND
C
C   CALCULATES AMPLITUDE VALUES IN THE MEDIUM
C
C   IN A PROFILE NORMAL TO THE INTERFACE
C
C * * * * *
C   VARIABLE DECLARATIONS AND DEFINITIONS
C
C   DENSITY OF MEDIUM
C
C   REAL RHO1
C
C   SPEED OF COMPRESSIONAL WAVES IN MEDIUM
C
C   REAL ALPHA1
C
C   SPEED OF SHEAR WAVES IN MEDIUM
C
C   REAL BETA1
C
C   INCIDENT ANGLE OF INCOMING SHEAR WAVE
C
C   REAL PHI1
C
C   FREQUENCY OF INCOMING SHEAR WAVE
C
C   REAL  $\omega$ 
C
C   RIGHT SIDE COEFFICIENT MATRIX
C
C   COMPLEX A(4,4)

```

C RIGHT SIDE VECTOR
 COMPLEX B(4)

C REFLECTION AND TRANSMISSION COEFFICIENT VECTOR
 TO BE CALCULATED
 COMPLEX C(4)

C SPATIAL POSITION WHERE DISPLACEMENT IS CALCULATED
 REAL X

C STIFFNESS TANGENTIAL TO INTERFACE PLANE
 REAL CT

C STIFFNESS NORMAL TO INTERFACE PLANE
 REAL CN

C DISPLACEMENT NORMAL TO INTERFACE
 COMPLEX Ux

C AMPLITUDE OF PARTICLE DISPLACEMENT
 REAL MUX

C SQUARE ROOT OF -1
 COMPLEX J

C TEMPORARY COMPUTATION VARIABLES
 COMPLEX Z, Z1, TEMP, TEMP1, TEMP2

C MODEL PARAMETERS
 ALPHA 1 = 8793.0
 BETA 1 = 3608.0
 RHO1 = .23*(ALPHA1**.25)
 PHI1 = 72.0*3.14159265/180.0
 ω = 2.0*3.14159265*2650

```
CN = -9.60E-15
CT = CN
J = (0.0,1.0)
C  COMPUTE ALL DISPLACEMENTS AT VERTICAL
C  DEPTH OF ZERO
X1 = 0.0
C  START DISPLACEMENT LOOP
DO 5 X=0.0, 5.00, .1
C  INPUT FREQUENCY INDEPENDENT COEFFICIENT
C  MATRIX ELEMENTS
Z=(SIN(PHI1)**2)-BETA1**2/ALPHA1**2
Z=SQRT(Z)
A(1,1)=Z
A(1,2)=Z
A(1,3)=J*SIN(PHI1)
A(1,4)=-J*SIN(PHI1)
A(2,1)=COS(2*PHI1)
A(2,2)=-COS(2*PHI1)
A(2,3)=-SIN(2*PHI1)
A(2,4)=-SIN(2*PHI1)
A(3,1)=2*J*Z*SIN(PHI1)
A(3,2)=2*J*Z*SIN(PHI1)
A(3,3)=-COS(2*PHI1)
A(3,4)=COS(2*PHI1)
C  INPUT FREQUENCY INDEPENDENT RIGHT SIDE
```

```

C    VECTOR ELEMENTS

      B(1) = -A(1,3)

      B(2) = A(2,3)

      B(3) = -A(3,3)

C    INPUT ALL FREQUENCY DEPENDENT TERMS

      Z1=CN*J/RHO1*W*BETA1

      A(4,1)=2*J*Z*SIN(PHI1)+Z1*SIN(PHI1)

      A(4,2)=-Z1*SIN(PHI1)

      A(4,3)=Z1*COS(PHI1)-COS(2*PHI1)

      A(4,4)=Z1*COS(PHI1)

      B(4)=-A(3,3)+Z1*COS(PHI1)

C    NOW ALL MATRIX AND VECTOR TERMS ARE

C    ENTERED CALL SUBROUTINE GAUS AND SOLVE

C    FOR REFLECTION AND TRANSMISSION COEFFICIENTS

      CALL GAUS (A,B,C)

C    NOW COMPUTE DISPLACEMENT FOR A GIVEN X

C    FIRST COMPUTE TEMPORARY VARIABLES

      TEMP=EXP(-(W/BETA1)*Z*X)*CEXP(J*(-W/BETA1)

1    *SIN(PHI1)*X1)

      TEMP1=CEXP(J*(-W/BETA1)*(X*COS(PHI1)+X1

1    *SIN(PHI1)))

      TEMP2=CEXP(J*(W/BETA1)*(X*COS(PHI1)-X1

1    *SIN(PHI1)))

C    COMPUTE DISPLACEMENT

      UX=C(1)*(-W/BETA1)*Z*TEMP-(J*(-W/BETA1)

```



```
1  *SIN(PHI1)*TEMP2)-C(3)*(J*(-w/BETA1)
1  *SIN(PHI1)*TEMP1)
C  COMPUTE MAGNITUDE OF DISPLACEMENT
   MUX=.114846206*ABS(Ux)
   WRITE(10,*) X, MUX
5  CONTINUE
   END
C  SUBROUTINE GAUS
   SUBROUTINE GAUS(AG,BG,XG)
   COMPLEX AG(4,4),BG(4),XG(4),SUM
C  EXECUTE FORWARD ELIMINATION SCHEME
   DO 300 K=1,3
   DO 200 I=K+1,4
   XMULT=AG(I,K)/AG(K,K)
   DO 100 J=K+1,4
   AG(I,J)=AG(I,J)-XMULT*AG(K,J)
100  CONTINUE
   BG(I)=BG(I)-XMULT*BG(K)
200  CONTINUE
300  CONTINUE
C  NOW BACK SUBSTITUTE
   XG(4)=BG(4)/AG(4,4)
   DO 400 I=3,1,-1
   SUM=(0.0,0.0)
   DO 500 J=I+1,4
```

```
      SUM=SUM+AG( I , J ) *XG( J )  
500  CONTINUE  
      XG( I )=(BG( I )-SUM)/AG( I , I )  
400  CONTINUE  
      RETURN  
      END
```